

A self-assembled periodic nanoporous framework in aqueous solutions of the DNA tetramer GCCG

Gregory P. Smith^a, Tommaso P. Fraccia^{b,c}, Chenhui Zhu^d, Tommaso Bellini^{b,2}, Noel A. Clark^{a,2}

^aDepartment of Physics and Soft Materials Research Center, University of Colorado, Boulder, CO, 80309-0390

^bDipartimento di Biotecnologie Mediche e Medicina Traslazionale, Università degli Studi di Milano, via Fratelli Cervi 93, I-20090 Segrate (MI), Italy

^cInstitut Pierre-Gilles de Gennes, Chimie Biologie et Innovation, ESPCI Paris, PSL University, CNRS, 6 rue Jean Calvin, 75005, Paris, France

^dAdvanced Light Source, Lawrence Berkeley National Laboratory, Berkeley, CA 94720 USA

²To whom correspondence may be addressed: noel.clark@colorado.edu

Abstract

The collective behavior of the shortest DNA oligomers in high concentration aqueous solutions is an unexplored frontier of DNA science and technology. Here we broaden the realm of DNA nanoscience by demonstrating that single-component aqueous solutions of the DNA 4-base oligomer GCCG can spontaneously organize into three-dimensional (3D) periodic mesoscale frameworks. This oligomer can form B-type double helices by Watson-Crick (WC) pairing, into tiled brickwork-like duplex strands, which arrange into mutually parallel arrays and form the nematic and columnar liquid crystal phases, as is typical for long WC chains. However, at DNA concentrations above 400mg/mL, these solutions nucleate and grow an additional mesoscale framework phase, comprising a periodic network on a three dimensional body-centered cubic (BCC) lattice. This lattice is an array of nodes (valence-8, each formed by a pair of quadruplexes of GCCG terminal Gs), connected with a separation of 6.6 nm by struts (6-GCCG-long WC duplexes). This 3D-ordered DNA framework is of low density (DNA volume fraction ~0.2), but, due to its 3D crystal structure, is osmotically incompressible over its phase range. Atomistic

simulations confirm the stability of such structures, which promise to form the basis of novel families of simply and inexpensively made nanoscale frameworks for templating and selection applications.

Introduction

The key role of DNA in biology stems from the selective interactions between the side groups (bases) on pairs of polymeric NA chains enabling matching sequences of large numbers of bases, N , to package and transmit genetic information. These structures are stabilized in solutions of arbitrarily small concentration, c , by the selective Watson-Crick (WC) adenosine-thymine and guanine-cytosine base-pairing motif [1], and by the columnar stacking in the duplex of the aromatic hydrocarbon nanosheets formed by the paired bases [2,3]. Nucleobases can also form and exploit non-WC bonds, among which are quadruplex strands of stacked guanosine tetramers (G4s), relevant for example in the functioning of telomers [4].

A more recent development has been the advent of DNA nanoscience, which has enabled the creation of an amazing variety of active and passive functional nanoscale structures via DNA oligomers self-assembled by similar base-pairing motifs. Appropriately designed combinations of NA strand lengths and base sequences can orchestrate programmed hierarchical self-assembly in solution on length scales ranging from nanometer to micrometer [5,6]. These biological and nanoscience application of NAs are generally based on self-assembly pathways which are operative at low concentration in aqueous solution, designed such that the specific intermolecular interactions are strong enough to bind single oligomers at very low osmotic pressure of the nucleic acid solutes. Among the workhorse themes of the resulting DNA nanostructures are frameworks [5,7], which are rigid, have low density, and present large surface area, attributes which combined with addressability and programmability form the basis for a broad range of chemical nanoscience applications. Here we achieve periodic framework fabrication via the self-assembly of a single species of 4-base DNA oligomer.

We have pursued in recent years a broad study of nucleic acids in the quite different regime where N is small, ($1 \leq N \lesssim 10$), and c_{DNA} is large, in the range $200 \text{ mg/mL} \lesssim c_{DNA} \lesssim 1200 \text{ mg/mL}$ [8,9,10,11,12,13,14,15,16,17,18]. At these concentrations, which are up to $\sim 2/3$ of that of dry DNA ($c_{DNA} \sim 1700 \text{ mg/mL}$) [19, 17], nucleic acids self-assemble into three dimensional collective structures and phases that depend on N , c_{DNA} , temperature, and the base sequences of the NA oligomers. Generally, as N is decreased the NA osmotic pressures and therefore the

concentrations required for collective self-assembly increase. In such solutions, where the oligomers are complementary or self-complementary, WC-like local organization and double helix formation can be obtained for any N , *i.e.* even $N = 1$, as in solutions of the monomer nucleotides [17]. The principally observed 3D self-assembly motifs that result are the packing of these duplex base-stacked columns into parallel arrays to form bulk nematic liquid crystal (LC) phases, or, at higher concentration, spontaneous arrangement of the columns on a hexagonal lattice to form columnar LCs, similar to that found in long DNA [20,21] at similar concentrations [8-17]. These phases are identifiable by x-ray diffraction and microscopic study of their birefringent optical textures [8,17].

This observation of WC duplex organization, in absence of the phospho-diester polymerization that stabilizes the double helix at low concentration, provides evidence for the hypothesis motivating the above-mentioned work, namely that LC spatial organization of single bases at high concentration could be a templating and selection mechanism for the appearance of double helical and polymeric nucleic acids in the approach to the RNA world in early life [15,16]. However, we have found that the small- N , regime also proves to be a rich area for the general exploration of novel soft-matter collective behaviors in NAs at higher concentrations. Here we report a nucleic acid system, obtained in single component aqueous solutions of the DNA tetramer 5'-GCCG-3', in which DNA can spontaneously assemble into a low-density 3D mesoscale framework of DNA rods, extending the horizon of nucleic acid nanofabrication to include components comprising a single molecular species, and ultra-short NAs.

The molecule investigated here is the DNA oligomer 5'-GCCG-3' in which the phosphodiester four-base chain is -OH terminated on both its 5' and 3' ends. We will refer to this molecule simply as GCCG. Synthesis, purification details are presented in Materials and Methods. Of the work cited above the most relevant to the results to be presented here is that of Ref. [14], our prior study of the four-base DNA oligomer 5'-GCCGp-3' (GCCGp), in which the phosphodiester four-base chain is -OH terminated on its 5' end, and -PO₄ terminated on its 3' end. In aqueous solution GCCGp presented the phase sequence [isotropic (ISO) – nematic (NEM) – columnar (COL)] with increasing concentration, a scenario similar to that found in solutions of longer $N < 20$ oligomers. However, in addition, GCCGp exhibited a second (reentrant) isotropic

(ISO2) phase at the highest c_{DNA} values, an observation not preceded in our earlier studies of hundreds of other oligomers. This ISO2 phase was tentatively proposed in Ref. [14] to be due to the formation of random networks of oligomer chains, driven by association of the terminal G's favored at high c_{DNA} .

The work presented here on GCCG was motivated by this observation, and by a basic theme emerging from our extensive exploration of $N < 20$ oligomers, namely that as N decreases their collective behavior becomes more and more sensitive to terminal composition. We report here that, while GCCG and GCCGp exhibit similar overall phase behavior, certain conditions enable GCCG to form a new "BCCX" mesoscopic framework phase that we analyze and understand to be a spontaneous cooperative ordering of a combination of WC and G4 molecular bonds. In order to facilitate GCCG – GCCGp comparison, GCCGp phase behavior is included with that of GCCG in *Fig. 1* and in the *Supplementary Information* as *Figs. S1* and *S2*.

The LC phases in these systems can be understood in terms of the WC "brickwork" duplex chaining mode of GCCGp and GCCG, sketched in *Fig. 2A*. and *Fig. S1*. In this chaining there is no distinction between duplex formation and linear aggregation. Rather, hybridization and chaining necessarily take place in a single continuous process, in which the bonding of each GCCG molecule to an existing chain (*Fig. S1B*) and the merging of different chains (*Fig. S1C*) are characterized by a free energy gain. This condition leads to equilibrium states characterized by a broad polydisperse distribution of lengths, ranging from single dissociated oligomers to multi-molecular aggregates with a characteristic length depending on interaction strength and temperature, T as generally expected in isodesmic self-assembly [22]. Rods which are polydisperse in length have a strong tendency to form nematic and columnar LC phases, the dominant LC phases observed here and in a large variety of $N < 20$ NA oligomer solutions [23].

Results

Exploration of the phase behavior of solutions vs. concentration c_{DNA} and T by depolarized transmission optical microscopy (DTOM) and x-ray scattering enabled division of the (c_{DNA}, T) plane into regions exhibiting distinct isotropic and birefringent optical domains characteristic of textures made by DNA LC phases, including the isotropic (ISO), nematic (NEM) and fluid

columnar (COL) [8,14]. The phase behavior was assessed by preparing solutions, of chosen DNA concentrations in the range $100 \text{ mg/mL} < c_{\text{DNA}} < 800 \text{ mg/mL}$, and filling them into planar glass cells or thin-wall x-ray capillaries. These solutions were made with or without added salt, the latter case making the corresponding native Na^+ counterion concentration in the aqueous partition $0.27\text{M} \lesssim c_{\text{Na}^+} \lesssim 3.9\text{M}$ in the above c_{DNA} range. Such fixed concentration samples were then temperature cycled at rates sufficiently slow to enable consequent formation of domains and concentration equilibration of the nematic and columnar phases. It is typical of DNA LCs that the transitions among these phases are first order. In addition, they are strongly hysteretic at the high concentrations being studied here (~5% to ~45% of neat DNA), conditions which combine to make regions of two- and three- phase coexistence quite common in the optical and x-ray cells. *Fig. 1B* shows the phase diagram of CGGC obtained from the optical and x-ray experiments, along with that of GCCGp in *Fig. 1A*, from Ref.[14], for comparison.

GCCGp and GCCG both exhibit the ISO phase of weakly aggregated oligomers at lower c_{DNA} and higher T , with the NEM and then the COL phase the first LC phases appearing with increasing concentration at lower T . In the GCCGp diagram of *Fig. 1A* the single phase regions are solid-colored, while two-phase coexistence areas are indicated in white. In the GCCG diagram of *Fig. 1B*, most of the diagram area exhibits two or three phases in coexistence. In this circumstance the concentrations of the coexisting phases (c_{phase1} , c_{phase2} , etc.) will generally be different from each other and from c_{DNA} , which sets the overall average. In both phase diagrams LC ordering is quite stable, found at higher temperatures and lower concentrations than in some longer blunt-ended oligomers (6-10mers) [8,9,12]. This is a result of the absence of the weaker A-T hydrogen bonding, the WC duplexes being stabilized exclusively by the stronger G-C bonding

Remarkably, in both CGGC and GCCGp the low concentration ISO phase range extends to the highest concentrations, a feature not found previously in any other short-DNA oligomer solutions, which typically form birefringent biaxial columnar liquid crystals of columnar crystals, at high c_{DNA} [8,9,12]. In GCCGp the ISO transitions subtly into a second isotropic phase, the ISO2p, which persists at high c_{DNA} upon cooling to room temperature. This high- c_{DNA} isotropic was attributed to the enhanced tendency for G-G-G-G tetra-base aggregation, promoted at high DNA concentration relative to CG base pairing by mass action, resulting in the formation of an isotropic

network gel of duplex strands cross-linked by G quadruplexes [14]. GCCG exhibits a quite similar phase scenario, clearly transitioning to a second isotropic phase (the ISO2) at high c_{DNA} . The ISO2p and ISO2 may or may not be the same phase.

However, by far the most striking and unexpected feature of the GCCG phase behavior is the large hatched (c_{DNA}, T) area in *Fig. 1B*, a broad range of temperatures at intermediate concentrations, in which a DNA phase is found that is at the same time crystalline and optically isotropic, a combination that is absent among the known phases of NA oligomers and polymers in solution. DNA crystals, such as those of the Drew-Dickerson dodecamer, for example [24], are built on the close packing of parallel extended WC duplex strands, and therefore have uniaxial or lower symmetry and are birefringent. Since this new phase is so unusual for single component DNA, we preview its structure in *Fig. 2*, as a guide for the detailed discussion of the experiments, evidence, and modeling leading to its discovery. X-ray and optical study of this isotropic GCCG phase, which we term the BCCX, shows that it is a three dimensionally (3D) periodic liquid crystal structure having the spatial symmetry of a body centered cubic crystal lattice. The BCCX lattice consists of octameric clusters of G's at the cube corners and center, connected into a network by WC duplex rods (struts) along the cube diagonals, each strut made of six GCCG molecules. The resulting cubic lattice is an open network structure, with a DNA volume fraction of ~ 0.2 (BCCX phase concentration $c_{BCCX} \sim 395$ mg/mL, including the Na^+ native counterions). This makes the BCCX the least dense of any of the LC phases it can coexist with in solution, enabling it to be readily separated by centrifugation.

This phase first appears upon extended incubation, over periods of ~ 1 day and longer, of GCCG samples in the hatched area of *Fig. 1B*. As c_{DNA} is raised above ~ 450 mg/mL with NaCl regulated to around 100 mg/mL, exhibited the growth of a population of isolated domains into existing NEM/COL textures. These scattering domains initially show up in the x-ray scattering as a distribution of localized resolution-limited bright spots in WAXS images (*Fig. 3A*), indicative of a randomly oriented distribution of what appear to be small single crystallites. The number and size of these crystallites increases with incubation time, and, as this happens it becomes clear that these spots are localized onto a set of rings, such that, as the volume fills with crystallites, the scattering evolves to give an x-ray powder pattern of rings (*Fig. 3B*). This pattern of scattered

intensity is circularly averaged around $q = 0$ to obtain the powder diffraction data in *Figs. 3-6*. The hatched area of *Fig. 1B* shows the range of stability of this powder scattering pattern once established, indicating, for example, that the underlying structure has high thermal stability. *Fig. 4* shows that this powder pattern exhibits a set of reflections that can be accurately Miller-indexed to the scattering expected from a body-centered cubic lattice of lattice parameter $a = 65.99\text{\AA}$ (space group #211, I432). The table shows that the calculated reciprocal lattice wave vector magnitudes $g_{(j,k,l)}$ ($g_{100} = 0.0952\text{ \AA}^{-1}$) agree very well with their corresponding experimental values $q_{(j,k,l)}$, for electron density wavelengths λ down to $\lambda \sim 10\text{ \AA}$, about 15% of the unit cell dimension.

As the BCC crystals are first forming at low $c_{\text{DNA}} \sim 400\text{ mg/mL}$, the BCC appears at multiple overlapping spacings that have nearly the same q -values, including diffuse rings with a shorter coherence length, observable in *Fig. 6*. However, with time and increasing c_{DNA} the final crystal phase was found to have this BCCX structure of *Fig. 2* over the entire hatched area, remarkably with a lattice parameter that exhibits no significant dependence on either c_{DNA} or T in this region, as illustrated in *Figs. 5,6*. The BCCX is resilient to temperature, retaining its structure to $T \sim 80^\circ\text{C}$ where it melts directly to the structurally disordered, and also optically isotropic, ISO phase. The ISO phase scattering $I(q)$ is featureless at $T = 92.2\text{ }^\circ\text{C}$ (*Fig. 5*), but scattering immediately returns upon cooling to the NEM phase, or at higher concentrations the COL phase, once again exhibiting the diffuse peak at $q \sim 0.2\text{ \AA}^{-1}$ ($T = 25.4\text{ }^\circ\text{C}$ in *Fig. 5*). *Fig. 5* reveals the hysteretic behavior of the BCCX, with the crystal failing to reappear through the process of supercooling the ISO by 60°C . Even more extreme hysteresis is found, in that at room temperature it can take many days for the BCCX peaks to reappear. *Fig. 6* shows that near room temperature the lattice disappears in a phase transition for $c_{\text{DNA}} \gtrsim 700\text{ mg/mL}$, the x-ray scattering becoming dominated by a diffuse ring at $q \sim 0.2\text{ \AA}^{-1}$, indicative of a phase transition to the positionally disordered ISO2 phase, which DTOM experiments show to also be optically isotropic. This combination of isotropy and short range order appears to be similar to that found in the high- c_{DNA} isotropic phase of GCCGp. [14].

Isolated growing crystallites pass through the stage shown in *Fig. 3* where they exhibit diffraction limited single crystal Bragg scattering that in many cases illuminates only single pixels in the scattering plane, requiring coherent scattering and defect-free BCC ordering of crystals of

thousands of unit cells . Discernable Bragg peaks persist in the powder averages only out to $q \sim 1.2 \text{ \AA}^{-1}$ (electron wavelength $\lambda \sim 5 \text{ \AA}$), indicating that few- \AA scale molecular position fluctuations must be reducing the peaks at larger q . A prominent feature of the x-ray diffraction by duplexed B-DNA is the on-axis base stacking peak at $q \sim 2 \text{ \AA}^{-1}$, which, in the LC COL phase, this is diffuse, such as in photo 51 [25] for example. This broadening is due to positional fluctuations of the base positions along the helix axis, making positional ordering along the helix short ranged. This also appears to be the case in the GCCG crystal in which the broadening of the base stacking peak is substantially stronger. Nevertheless the BCCX is a crystal phase, a relative of the blue phases - arrays of topological defects in a chiral nematic liquid crystal director field that is everywhere fluid, spontaneously appearing and organizing into a cubic lattice. They are crystals without any atomic-scale positional order.

The lack of concentration dependence of the BCCX in *Fig. 5* can be usefully contrasted with that of the NEM and COL phases of GCCG presented in *Fig. SI9* and also visible in *Fig. 6*, which shows that as concentration c_{DNA} increases, q_p , the position of diffuse scattering near $q_p \sim 0.2 \text{ \AA}^{-1}$, indicating that the sample contains a residual fraction of coexisting COL phase, also increases (blue crosses). This phenomenon reflects the fact that upon increasing c_{DNA} , the double helical columns, incompressible in length, get closer sideways. This behavior is found in long duplex DNA [26,27], complementary dodecamers [8] and shorter oligomers [28].

Reduction of intercolumnar distance can be produced by controlling either the DNA concentration or the DNA osmotic pressure directly [29], the latter showing that h data can be used to read out DNA osmotic pressure. Accordingly, by showing the growth of density in the coexisting COL phase, data in *Fig. SI9* demonstrate that BCCX structure withstands the increasing osmotic pressure, a behavior coherent with its crystalline structure. From the intercolumnar distance, by a simple construction (*SI Section SI3*) we estimate that the osmotic pressure, P , in the investigated interval ranges from $P \sim 2$ to ~ 5 MPa over the range $400 \text{ mg/mL} \lesssim c_{\text{DNA}} \lesssim 700 \text{ mg/mL}$. Over this range *Fig. 6B* shows a fractional compression of the BCCX lattice of $s = \delta a/a < \sim 0.3\%$, and therefore an estimate of the BCCX lattice bulk modulus is $B \sim P/s \sim 10^9 \text{ Pa} = \sim 10^4 \text{ atm}$.

Model

We considered the modes of NA self-assembly which could lead to a low density, nearly incompressible, crystalline structure, starting from the following observations: *(i)* Since the lower temperature region of the BCCX phase in *Fig. 2* is occupied by the columnar phase, we assume that the basic self-assembly motif of GCCG will be into G-C complementary base-paired “brick-work” duplexes. Such fiber-like columnar aggregates create the mechanism by which rigid, low density structures can be made; *(ii)* Such duplexes of finite length terminate with GC tails at the two ends; *(iii)* The ability of G to interact with monovalent cations to form G4 structures is very well known [30]. Stacked, two or three-layered G4 offer the possibility of linking 8 or 12 duplex assemblies by coupling their tails together. It is important to note that the native Na⁺ cations are present in sufficient quantity in GCCG solutions ($c_{\text{Na}^+} = 1.34\text{M/L}$ at the BCCX concentration) to render the DNA non-acidic and, with the three phosphate groups in GCCG, there are always enough cations around to form every G in the material into a quadruplex; *(iv)* Side-by-side intercolumn interactions must be largely irrelevant in the determination of crystal structure and lattice parameter. *(v)* The lack of dependence of BCC lattice parameter, and therefore the BCCX structure on solution concentration c_{DNA} or temperature is indicative of a nearly fixed BCCX concentration, c_{BCCX} . *(vi)* Centrifugation experiments indicate that the density of the BCCX phase, c_{BCCX} is less than $\sim 450\text{ mg/mL}$, which is much less than the solution concentration c_{DNA} over most of its concentration range.

The simplest models for the BCCX incorporating considerations *(i)* to *(vi)* involve the formation of 3D open frameworks built by connecting finite-length WC base-paired duplex rods (struts) by nodes formed from groups of CG tails at their terminal ends through G4 motifs as in *Figs. 2,7*. We have constructed what we consider to be an exhaustive set of such models, subject to the constraints imposed by the XRD-indicated BCC crystal structure, the optical isotropy, and the measured BCCX lattice parameter a . In these models the nodes are centered at points of cubic point group symmetry, having on average the point symmetry elements of an octahedron. The instantaneous electron density distribution within a G4 node at any given time will be of lower symmetry than this, but the average requirement for node structure can be most readily modeled by making them spherical and of uniform density, as the simplest approximation. The resulting

lattices are shown in *Fig. 7*, wherein each strut comprises a WC paired region of length s that inserts its CG terminations into nodes of radius r at either end, the total length of the strut being $d = 2r + s$, where d is the node center separation. In the case of struts parallel to the cube edges or parallel to the diagonals we have $d = a$ or $d = (\sqrt{3}/2)a$, respectively. r and s depend on the valence N of each node, i.e. the number of GCCG terminals converging in it, and on the number M of GCCG oligomers present in the strut, respectively. r can be estimated assuming the node to be spherical and completely filled with DNA of uniform density ρ_{DNA}

$$r = \left(\frac{3Nm_{GC}}{4\pi\rho_{DNA}} \right)^{\frac{1}{3}}, \quad (1)$$

where N is the number of GC units in a node, m_{GC} is the mass of a single-stranded GC element, (about $\frac{1}{2}$ the mass of a full GCCG oligomer - MW = 1171.8 g/mol) and $\rho_{DNA} = 1687$ mg/mL, the density of dry long DNA. The value of s can similarly be calculated as $s = 3.39(2M - 2)\text{\AA}$ from the known WC inter-base stacking distance that we take that to be 3.39\AA based on our x-ray observations of nanoDNA in B-form WC columnar stacks.

The BCCX can be built by constructing a simple cubic lattice of unit cells of edge a and dressing them with a 2-node sites form factor at a cube corner and the cube center, with their connecting strut, in each unit cell. There are three lattices compatible with this node-strut structures and with the BCC symmetry. As sketched in *Fig. 7*, they feature a node at one corner of the unit cell (UC) and another at the UC center. We jointly varied N and M to obtain BCC unit cells with $a \sim 66\text{\AA}$, and calculated the resulting concentration of the phase in mg/mL, including Na^+ counterions. Lattice #1 (L1) places two sets of struts parallel to the UC edges, one running through the UC corner and the other through the UC center, creating an interpenetrated pair of simple cubic lattices, where the cube corners of one lattice are at the cube centers of the second lattice. In L1 the node valence is $N=6$ and the condition $a \sim 66\text{\AA}$ yields $M=8$. L2 places the struts along the diagonal lines between the corner of the UC and the center of the UC. In L2, $N=8$, a structure compatible with a two-layered G4 assembly and $M=6$. L3 merges these two models, with struts along the edges of the UC as in L1, but also along the diagonals of the UC, as in cell L2. In L3 the node valence is $N=14$ and the strut length is either $M=6$ or $M=8$ depending on their direction with respect to the BCC axes. *Fig. 7A-D* and the table summarize the characteristics of

these lattices. L1 and L2 give concentrations $c_{\text{BCCX}} = 351$ and 396 mg/mL, respectively, both satisfying the condition of consideration (v) above, whereas L3, due to its much higher concentration, can be eliminated on this basis. In L1 and L2, with 48 GCCG oligomers per UC volume of a^3 , the native Na^+ ion concentration in the aqueous solvent of the BCCX crystal is 1.34 M/L. Condition (iii) enables discriminating between L1 and L2 since only the latter has a node valence multiple of 4.

We further examined the nature of such BCCX lattice assemblies using atomistic molecular dynamics simulation. Run times available for atomistic simulation of the BCCX system were not of sufficient duration to model large-scale collective behavior, for example crystal self-assembly starting from a disordered state, but could be effectively used to probe structure and fluctuations within a node under circumstances typical of its tethering by the struts in a BCCX lattice. To this end, we carried out simulation runs starting from the state shown in *Figs. 8, S4*, in which a BCCX network element is built using 48 5'-GCCG-3' oligonucleotides. These are arranged to form eight B-type DNA duplex struts, each six oligonucleotides in length, all terminated at one end on a single node. We searched in the literature for nonplanar H-bonding modes of the Gs that might enable a node assembly with octahedral symmetry but did not find suitable candidates, so we settled for eight G's in a standard pair of stacked quadruplexes. In the BCCX both 3' and 5' ends populate the nodes, but for this simulation all of the struts have their 5' terminations in the node. The eight struts were arranged to radiate out toward the corners of a cube centered on the G-quartet pair, forming an eight-armed star with the node at the center. This starting assembly was immersed in water with the native sodium counterions, then simulated in X, Y, Z periodic boundaries using the Amber force field on the Gromacs simulation package. This gave a simulation containing 48 GCCG oligomers, 13990 water molecules and 144 sodium cations (48119 centers total) with initial dimensions of the periodic box of $8.4 \times 8.4 \times 6.9$ nm. During the 20 nsec simulation runs the stars did not penetrate the box boundaries, so they were fluctuating independently, effectively as if in an infinite medium. Simulations were carried according to the procedure in the *Supplementary Information*.

Analysis of simulations of 20 nsec runtime showed the following: (i) In the struts, the GCCG WC brickwork duplex tiling structure is maintained, with fluctuations. *Fig. S10* shows

that the advance of the helix twist angle per base in the struts is nearly same as that of average long double helix B-DNA; (ii) In the node, the mean duplex stacking structure of a pair of G-quadruplexes is maintained for at least 20nsec, although with fluctuations that can be as large as having a G transiently decoupled from the eight-G cluster, as in *Fig. 9C*; (iii) In a node the C's in the -CG tails form a $r \sim 26 \text{ \AA}$ diameter quasi-spherical shell around the G-quadruplex core; (iv) The C's in the -CG tails tend to maintain a single base-stacking contact with either their struts or with the G-quadruplex core. (iv) The simulations show that the assumption of *Eq. 1* that the node density is that of neat DNA, *i.e.*, that water is expelled from the sphere of radius r containing the -CG terminal groups, is likely to result in an underestimation of r , relative to the experimental value. Thus the simulations show that the packing of the -CG terminal groups in node core is not effectively space-filling, such that the -GC DNA is not dense and the node contains a significant amount of water, making its volume, and therefore r , larger than that given in *Eq. 1*. Since, according to *Fig. 7*, r contributes to the lattice parameter a , the use of r from *Eq. 1* should make the lattice parameters calculated from the model smaller than experimental values. The table in *Fig. 7* shows this to be the case only for L2, for which the model $2r = 20.6 \text{ \AA}$ and model $a = 63 \text{ \AA}$ while the effective $2r = (2/\sqrt{3})a - s = 23.6 \text{ \AA}$ from the experimental $a = 65.99 \text{ \AA}$ and model s . The approximate L2 node diameter from the simulation can be determined from *Figs. 9, S5-S8* to be $2r \sim 25 \text{ \AA}$. As noted above, a stacked quadruplex node assembly will not be consistent with the point symmetry of the BCCX lattice for any orientation, but achieves the lattice symmetry on the average. As a result the BCC crystal should exhibit diffuse scattering coming from orientation fluctuations of its G quadruplexes.

Discussion

A rough estimate of the relative stability of the COL and BCCX phases can be made by considering the free energy change ΔG produced upon introducing breaks in GCCG duplex chains, generating free ends with unstacked and unpaired Gs. In the case of L2 this involves making four such breaks and then inserting the 8 terminal Gs into node balls, within each of which they form a two-layered (2L) G4 stack. The free energy gain ΔG_{2LG4} involved in the formation of the 2LG4, must overcome the loss for the 4 breaks, each of which involves the loss of 3 nearest-neighbor stacking contribution ΔG_{NN} , that we can evaluate using the conventional tools for the thermal stability of DNA duplexes [31]. In the evaluation we should also consider the 2LG4 stabilizing contribution ΔG_{DE} due to the “dangling end” stacking of the unpaired C to the WC-bond portion of the struts:

$$|\Delta G_{2LG4}| > |12\Delta G_{NN} - 4\Delta G_{DE}| \approx 4 \times \left(3 \times 2.3 \frac{\text{kcal}}{\text{mol}} - 0.75 \frac{\text{kcal}}{\text{mol}} \right) - 8 \times 0.5 \frac{\text{kcal}}{\text{mol}} \sim 20 \frac{\text{kcal}}{\text{mol}}, \quad \text{Eq. 1}$$

where the second term in parenthesis is the correction for salt concentration [31]. The resulting $\Delta G_{2LG4} > 20$ kcal/mol is compatible with the free energy measured for the assembly of two layered G4 [32,33], although it should be noted that the 2LG4 structure we are here considering differs from the ones used to determine the free energy available in literature, based on G4 forming within oligomers containing repeats of guanines. We suggest that the free energy associated to the BCCX 2LG4 formation could be larger than the literature values, since the association of 8 chemically independent chain terminals, unconstrained by chain loops as in the G4-based secondary structures of oligomers, benefits from a larger conformational freedom, enabling guanines to relax to their position of strongest stacking. Indeed, ΔG_{2LG4} should not only satisfy the necessary stability with respect to the COL phase, expressed in Eq.1, but also provide the free energy required by the collective rigidification inherent in the assembly and structuring of a 3D crystal lattice, in which fluctuations are certainly quenched with respect to the COL phase with equal c_{DNA} . This notion combines with the observation that the BCCX structure is not found in GCCGp, where the terminal phosphates destabilize the 2LG4 nodes by adding an element of electrostatic repulsion, and with the fact that BCCX does not appear in conditions of lower or larger ionic strength, both suggesting that the stability of BCCX is marginal, where the free energy gained in forming the 2LG4 nodes is entirely spent in the stabilization of the BCCX structure.

We argue that collective rigidification is also at the origin of the large thermal stability of BCCX, whose melting is 30°C above that of the COL phase despite the smaller c_{DNA} . The stability of BCCX mainly depends on that of the WC struts, being these the weakest bonds in the structure. Thus, the huge increment in their stability with respect to the COL phase must be a consequence of an increment in the free energy associated to the GCCG WC bonding that can be attributed to a reduction of the entropy penalty for their formation, in turn suggesting a significant reduction of bond-breaking fluctuations of the BCCX struts compared to that in COL columns, with the each .

The observation of the BCCX phase brings with itself the two questions of why it is present in the GCCG phase diagram only, never having been observed in our previous studies of more than a hundred LC-forming DNA oligomers [8-18], and why the lattice parameter adopted in the BCCX requires 6 GCCG molecules in the WC bonded struts. While we do not have a definite answer to the question, *Fig. S10* introduces an element of strut structure to be considered, namely that the strut length for the spontaneously chosen lattice parameter is close to that of a complete turn of the double helix, the latter assessed from the atomistic simulations (*Fig. S10*). This enables the possibility that for a given strut each strut-end would approach coupling into its G-aggregate with the same average orientation relative to the crystal lattice directions. We argue that any correlation among the azimuthal angles of the WC duplexes at the 2LG4 nodes would tend to favor struts of length equal to a multiple of the WC B-DNA helical pitch. At the same time, longer WC struts would have markedly reduced thermal stability since in larger BCCX unit cells the crystal-induced structural stability and fluctuation reduction would be much less. Thus $M=6$ could be the sweet spot combining short WC aggregate with a complete helical turn.

Along these lines, a good candidate for exploration would seem to be “sDD”, the 12-base oligomer of sequence GCGCGCAATTGC [34,35] that is self complementary with GC overhangs, and whose hybridization leads to chemically continuous structure of length and terminals matching those of the $M=6$ GCGC struts. However, our limited studies to date of sDD have not revealed a BCCX phase. This could very well be a consequence of the kinetic barrier involved in the formation of such a phase. Indeed, even in the weakly bonded, highly dynamic GCCG solutions, nucleation of BCCX encounters a significant barrier. Given that the local melting attempt rate

should be much higher in GCCG than in sDD, sDD-BCCX nucleation might be many orders of magnitude slower.

Conclusion

While there is an ample literature reporting the self-assembly and secondary structuring of NA oligomers based on WC or G4 binding modes, examples of structures based on their combination are missing. The nanoporous crystalline BCCX scaffold adopted by GCCG as its favored equilibrium state in a large range of its phase diagram is a rare example of a mode of association crucially depending on both. We find BCCX to form via nucleation in solutions already collectively organized through WC pairing. In these, G-C base-pairs are built quickly given a rate equation that involves only two components, but they are not as stable, while G-multimer structures, like G-quartets, are highly stable but slow given a rate equation that may involve eight parts at once. Base-pairs formed early can be reversed slowly over time and replaced by G-quartet-like associations to create structures that contain both regions of WC base-paired helix and stacked G-quadruplex.

It is intriguing that the smallest nanoDNA oligomers also tend to have the most diverse phase behavior in the DNA family. Indeed, longer oligomers tend to have a definite preference for WC or G4 mode of assembly, driven by the cooperativity in the H-bonding of chains, and by the tendency for kinetic arrest of base-paired chaining into long-lived duplex strands [11]. By contrast, small oligomers like GCCG tend to spend their time in short-lived assemblies, thereby exploring more effectively the possibilities of their phase space, *i.e.* they sample WC assembly but doing so does not lead to a double helix dead end.

The combination of multivalent nodes and linear connectors is a basic design for soft, porous, three-dimensional reversible networks in soft matter, often appearing in the form of hydrogels. Such networks are typically formed by the association of complex units that control the valence and the internode-spacing [7], or they result in very disordered structures [36]. Only by highly complex monomer design these networks can achieve long range periodicity [5]. The GCCG self-assembly reported here expands the realm of soft matter and DNA nanoscience to include periodic, nanoporous networks by self-assembly in systems of single component, and

ultra-small, molecules. The WC strut and G4 node motif introduced appears to have potential for use as a general structural theme for the self-assembly of mesh-like framework nanostructures.

Figures

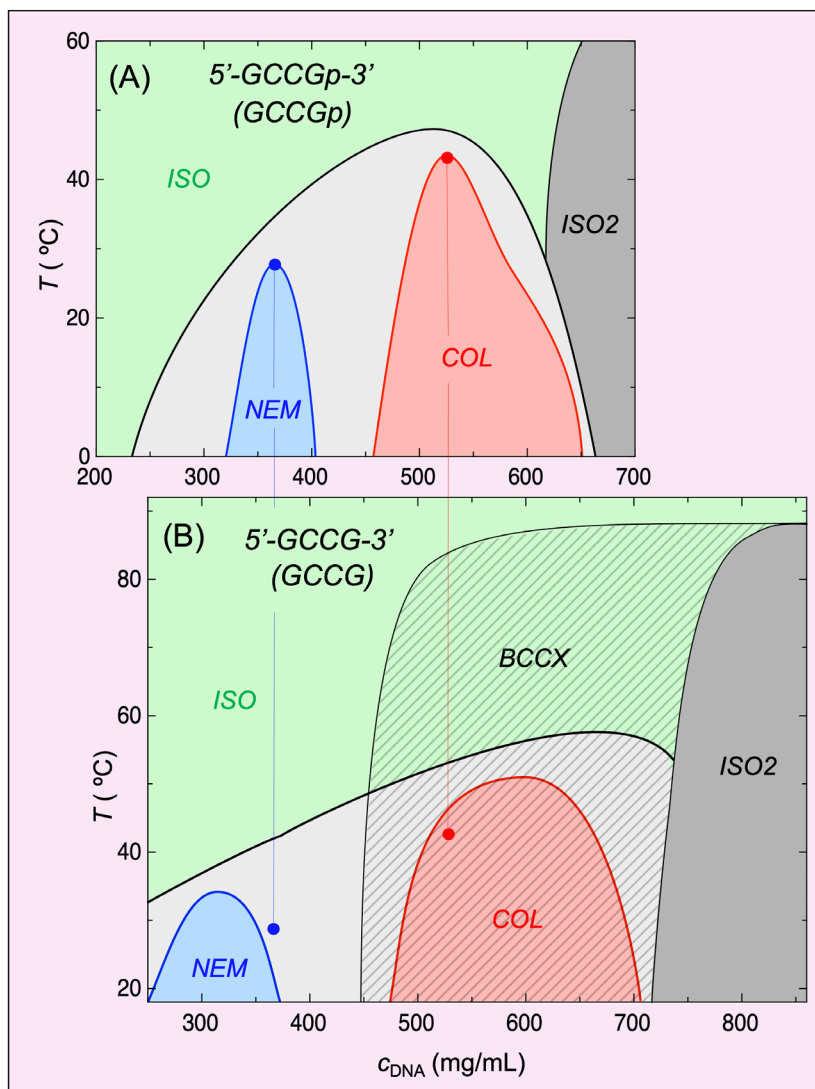


Figure 1: Concentration, c_{DNA} , versus temperature, T , phase diagrams for G-C DNA 4mers 5'-GCCGp-3', terminated at 3' by a phosphate group, reported in [Ref. 12], and 5'-GCCG-3' terminated at 3' by an undecorated hydroxyl, reported here. Concentrations range up to 800 mg/mL, which is ~50 weight% DNA. The solid dots indicate, on both phase diagrams for comparison, the highest T of the NEM and COL ranges of GCCGp. (A,B) Liquid crystal phases observed in both oligomers at these high concentrations are the isotropic (ISO, green), high concentration isotropic (ISO2, gray), nematic (NEM, blue), and uniaxial columnar (COL, red), with regions of phase coexistence among these (white). (B) In addition, 5'-GCCG-3' exhibits a

low-density body-centered cubic crystal phase (BCCX), which is broadly coexistent with the other phases in the hatched region ($\sim 450 \text{ mg/mL} < c_{\text{DNA}} < 800 \text{ mg/mL}$ $T < \sim 85^\circ\text{C}$).

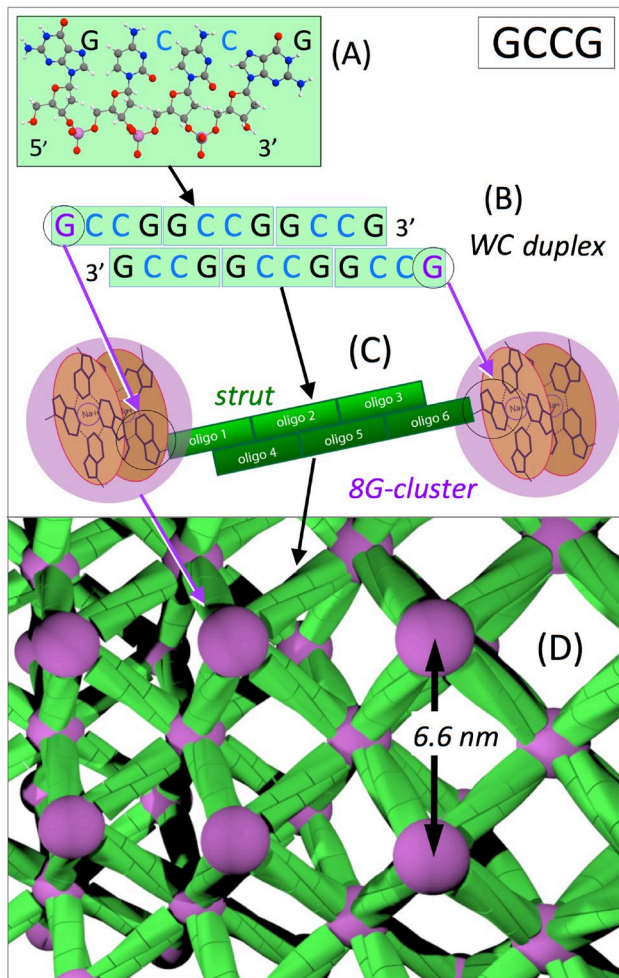


Figure 2: View of the hierarchical structural organization of our model of the BCCX phase of 5'-GCCG-3' (GCCG), introduced as a guide for the detailed discussion of the experiments, evidence, and modeling. (A) A schematic 5'-GCCG-3' oligomer containing Guanine (G), Cytosine (C) and three deprotonated phosphates in the deoxyribose phosphodiester backbone. (B) Oligomers assemble by Watson-Crick (WC) base pairing and stacking into linear duplex columns comprising a brickwork tiling of oligomers, with each duplex pair producing GC overhangs on both its 5' and 3' ends. (C) The GC-terminated duplex columns aggregate by guanine-to-guanine association into star-like clusters stabilized by the formation and stacking of G-quartets in G-rich nodes. (D) Duplex struts of WC base paired oligomers bridge between the nodes to form a periodic BCCX framework phase with struts and nodes on a body centered cubic crystal lattice having a lattice parameter $a = 6.6$ nm, and a DNA concentration $c_{\text{BCCX}} = 396$ mg/mL.

This drawing gives a qualitative representation of the BCCX electron density in which sub-5Å structure is smoothed out by fluctuations.

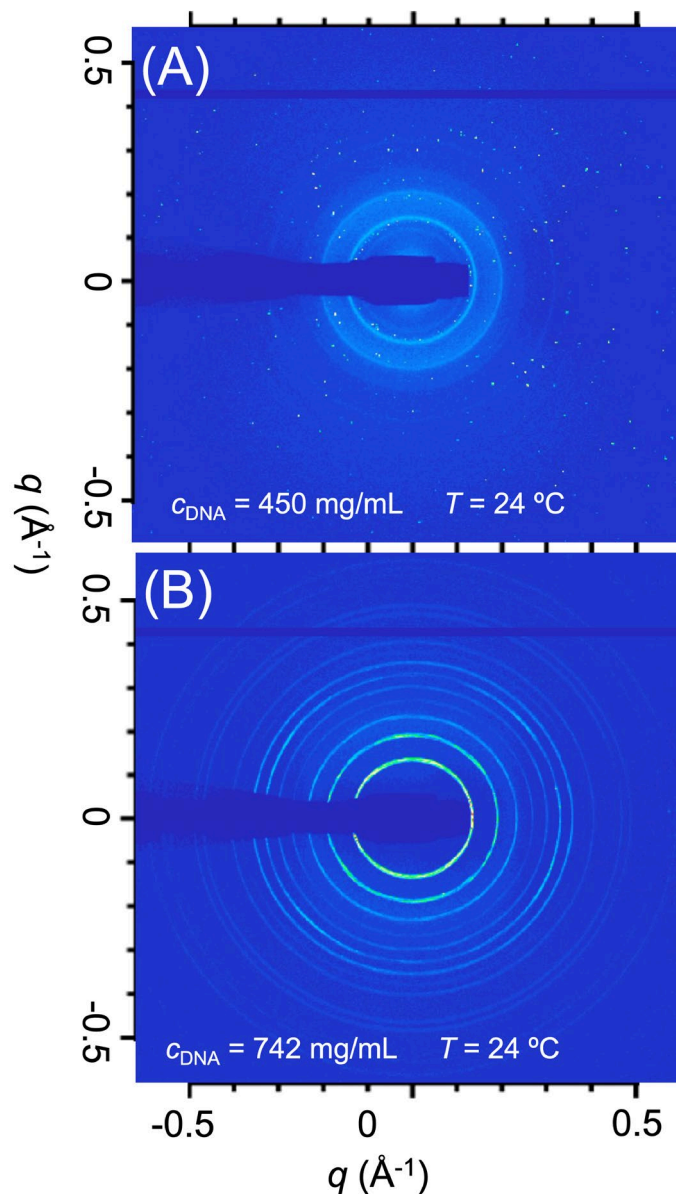


Figure 3: The small angle region of 2D WAXS x-ray diffraction patterns obtained from the 5'-GCCG-3' BCCX phase, forming or having formed from GCCG starting solution exhibiting coexisting NEM and COL phases. (A) BCCX growing in as isolated crystallites at $T = 24^\circ\text{C}$ and $c_{\text{DNA}} = 450 \text{ mg/mL}$. At this growth stage scattering from a single crystallite typically illuminates only a single pixel in the scattering plane. This diffraction-limited scattering requires perfect single crystal domains containing a minimum of $\sim 10^3$ unit cells of 6.6nm dimension – evidence for crystalline ordering. The diffuse rings are produced by both the NEM and COL ordering in the starting solution, as well as BCCX-like structures having only short-ranged ordering. (B)

Annealed powder scattering pattern obtained at higher concentration. Absence of diffuse scattering indicates that the BCCX phase has filled the sample volume.

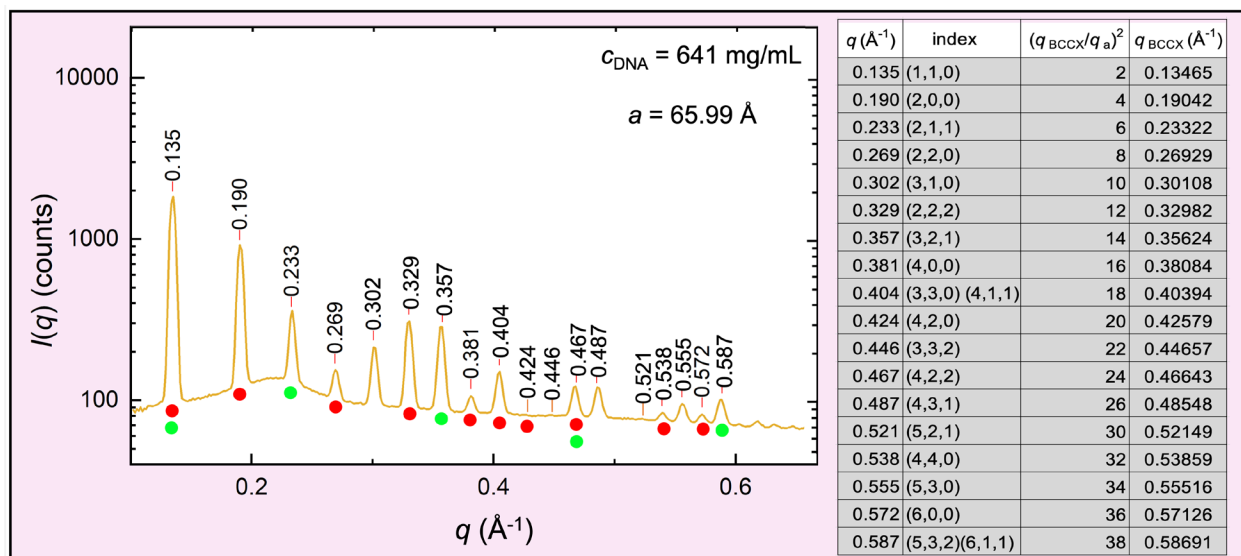


Figure 4: Radial scattered intensity scan $I(q)$ obtained by circular averaging a typical powder scattering pattern of the kind shown in *Fig. 3B*, and its indexing to a face centered cubic (FCC) reciprocal space lattice (body centered cubic (BCC) crystal real space lattice). Diffraction peak locations are annotated in $q(\text{\AA}^{-1})$, and each line in the accompanying table shows a measured q -position value, its Miller index assignment on the FCC reciprocal lattice, the ratio of that q_{hkl} magnitude to the simple cubic lattice vector $q_{100} = 2\pi/a$, and the resulting q_{hkl} values calculated for this indexing and a unit cell dimension of $a = 65.99\text{\AA}$. The plot and table show a complete 1:1 match of FCC reciprocal lattice points with data peaks in $I(q)$, out to $q = 0.6 \text{ \AA}^{-1}$. Colored spots indicate which peaks would be present for BCC lattices made up from arrays of featureless, infinitely long rods: *RED* – Rods along all of the cubic unit cell edges; *GREEN* - Rods along all of the cubic unit cell diagonals.

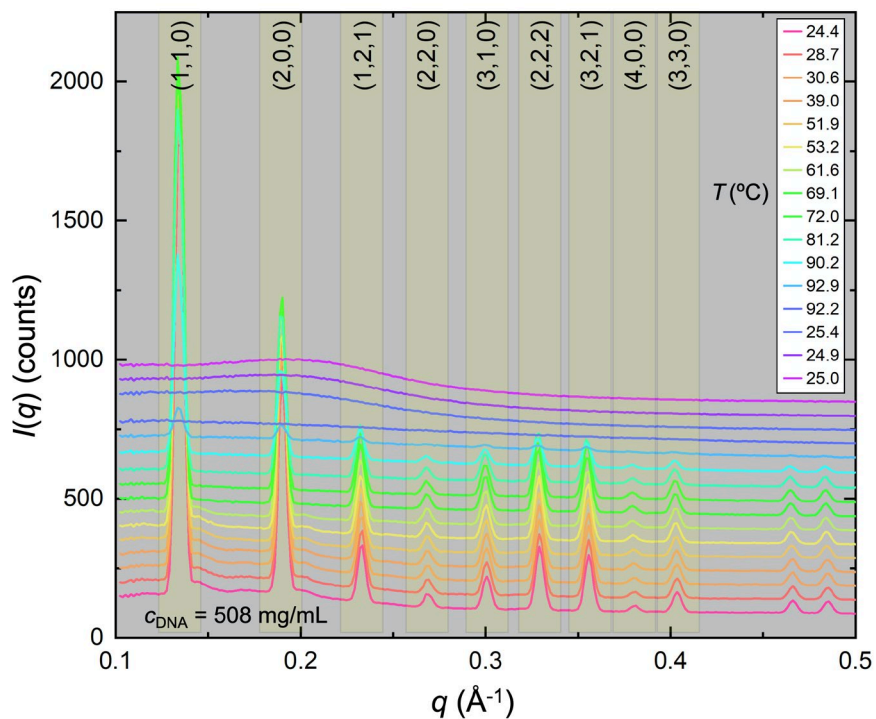


Figure 5: X-ray diffraction of the BCCX phase of 5'-GCCG-3' at $c_{\text{DNA}} = 508 \text{ mg/mL}$, for steadily increasing temperature. The Miller indices from **Fig. 4** are indicated. The BCCX is seen to persist to $T \sim 90 \text{ }^\circ\text{C}$ (cyan), melting temperatures that are much higher than those of the duplex columnar NEM or COL phases in GCCG in **Fig. 1**, or even in other longer DNA oligomers [6-16]. Since the BCCX crystal structure requires intact duplex struts, these high melting temperatures show that the connectivity of the BCCX network structure stabilizes the WC strut assemblies. Upon melting the BCCX x-ray pattern gives way to the featureless scattering of the ISO (blue), but the diffuse columnar peak from side-by-side columnar packing in the NEM phase appears upon cooling, and persists to room temperature (magenta). It may take hours, days, or weeks for the BCCX crystals to reappear.

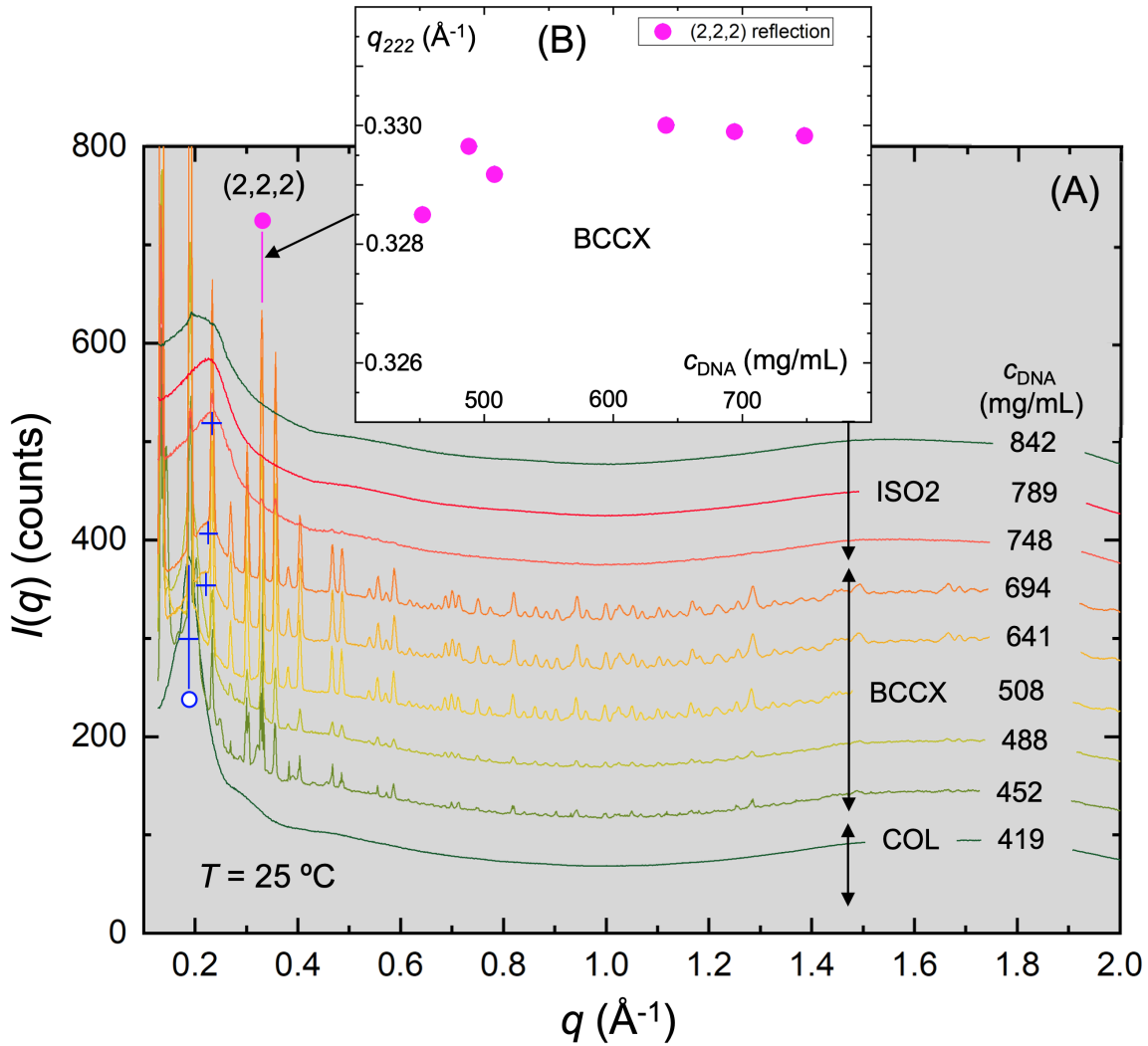
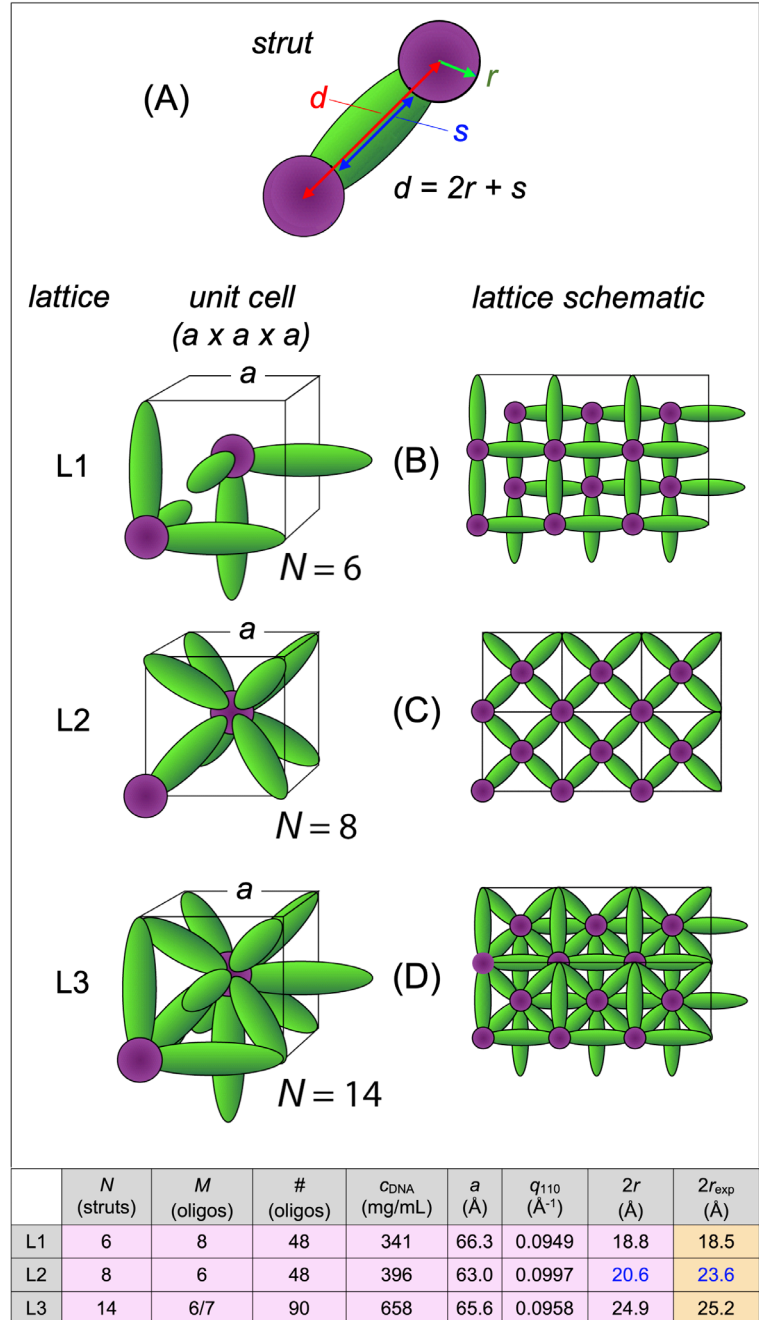


Figure 6: X-ray diffraction at room temperature for a broad range of 5'-GCCG-3' concentrations that includes the BCCX phase. (A) Low concentration phases are at NEM/COL coexistence and the BCCX is seen for $450\text{ mg/mL} < c_{\text{DNA}} < 700\text{ mg/mL}$, with a coexisting COL phase also in this range (COL peaks denoted by blue +). The BCCX gives way to the ISO2 at the highest concentrations, the latter exhibiting a nematic-like correlation peak at $q \sim 0.2\text{ \AA}^{-1}$, but without birefringence. In (A) there appears to be little change in BCCX Bragg peak positions with increasing c_{DNA} . This is quantified in the inset (B) which shows fitted positions of the BCCX $q_{2,2,2}$ Bragg peak vs. c_{DNA} , yielding a $\sim 0.3\%$ fractional contraction of the BCCX lattice with increasing c_{DNA} over the total BCCX range. The COL peaks (blue+, plotted as open circles in Fig. S9) shift to larger q with increasing c_{DNA} , indicating an increase of $\sim 3\text{MPa}$ in the DNA osmotic pressure over

the BCCX c_{DNA} range. If it is assumed that it is this compression that produces the 0.3% lattice contraction, then the BCCX crystal bulk modulus can be estimated to be $B \sim 10^9$ Pa.

Figure 7: Possible node-strut lattice models for BCC lattices that fit the x-ray data. (A) Schematic of strut structure, each strut consisting of a WC base paired region with a length s (green) terminated on either end by perfectly spherical, ideally space-filling nodes containing single-stranded segments of Guanine and Cytosine with a radius of r (purple). The node-center to node-center length of a strut is therefore $d = s + 2r$ including penetration into the nodes at either end, such that s depends on both node volume and node-center separation. All lattice parameters are calculated under the premise that the WC regions are duplex DNA stacks with 3.4 Å base pair spacing and that the nodes have an nominal DNA concentration of 1687 mg/mL. The table summarizes the parameters for the specific lattices



considered. (B) *Lattice model L1* – Nodes have $N = 6$ Gs, struts have $M = 8$ GCCGs and are parallel to the cube edges, forming two inter-penetrating cubic lattices linking cube corners, and the unit cell has 48 GCCGs. (C) *Lattice model L2* – Nodes have $N = 8$ Gs, struts have $M = 6$ GCCGs and are all diagonal, linking cube center nodes to corner nodes, and the unit cell has 48 GCCGs. The $M = 6$ struts have WC double helix runs of 10 bases, making the strut length nearly the same as the helix pitch. (D) *Lattice model L3* – A combination of lattices L1 and L2 where nodes have $N = 14$

Gs, diagonal struts have $M = 6$ GCCGs, edge struts have $M = 7$ GCCGs., and the unit cell has 96 GCCGs.

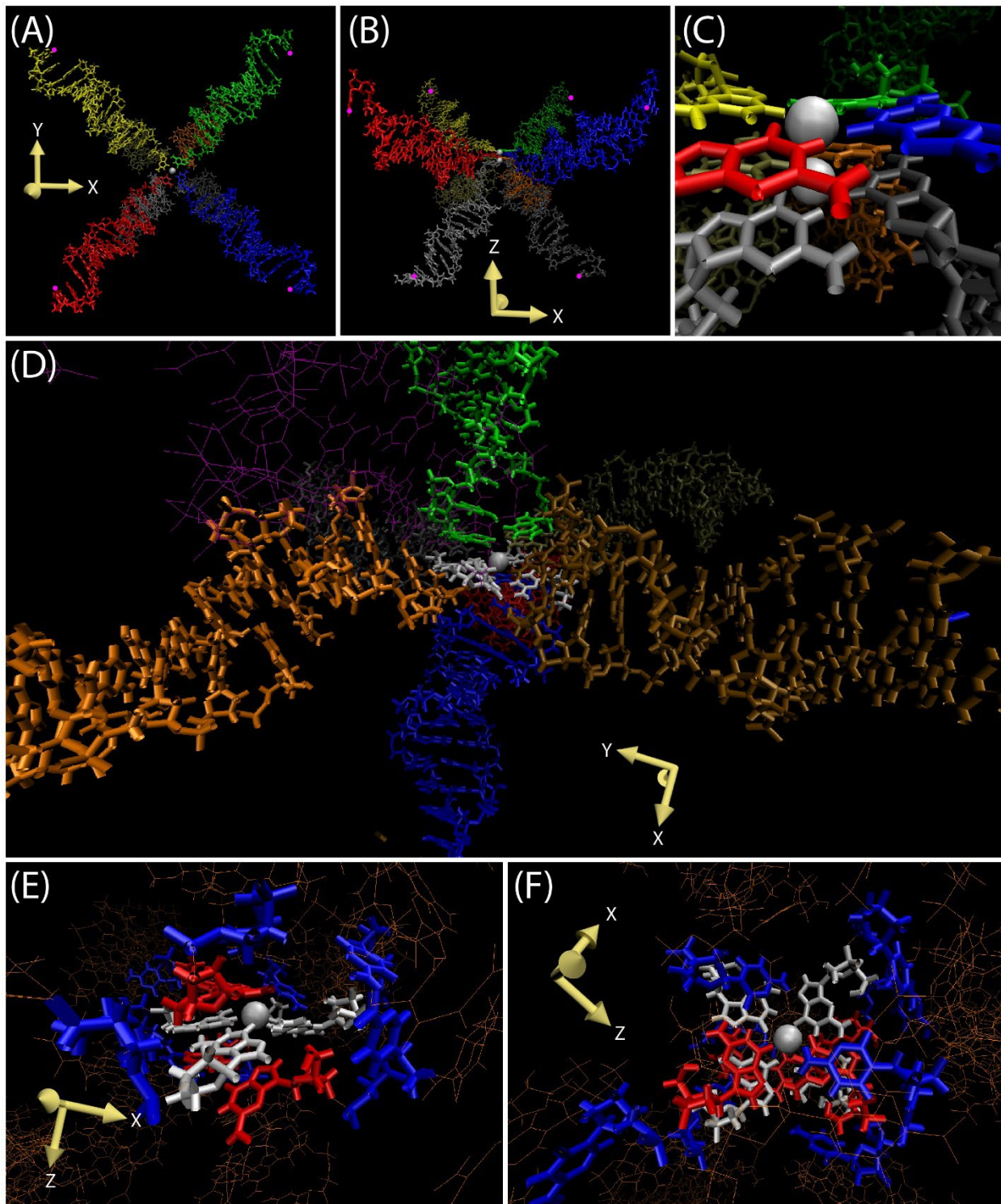


Figure 8: Atomistic molecular dynamics (MD) simulation of an eight-arm star representing a single node in an L2 lattice. The star is formed by a node having $N = 8$ Gs and 2 sodium atoms (gray spheres), with eight $M = 6$ struts projecting out toward the corners of a $ZZ\text{\AA} \times ZZ\text{\AA} \times ZZ\text{\AA}$ simulation unit cell. (A-C) Views of the starting geometry of the simulation, which has the node structured as a 2-layer G-quadruplex stack in the x - y plane, each with an Na atom at its center. The struts are pinned at their ends to the corners of a cube matching the dimensions of the XRD lattice unit cell, by weak single-atom restraints on an oxygen atom in each of the terminal G-residues (magenta circles). (D) State of the node system at the end of a $t = 150$ ns simulation run at 293 K. The forward struts are colored orange, violet, green, blue and ochre while the rear struts are red, brown, gray and silver. The violet strut is rendered in wireframe to facilitate visibility of the node. The node itself at this time point comprises a single G-quartet (white) with one trapped sodium ion, the other sodium ion having escaped in the first 10 ns of simulation. The final G-quartet involves guanines taken from both of the original quartets. (E) and (F) show the 150 ns node structure from other directions. The core of the node is a single G-quartet (white) around a sodium ion (gray) forming a hydrophobic nucleus upon which additional free bases are stacked; including terminal guanines (red), unpaired cytosines (blue), and some additional guanines and cytosines originating from the 3' terminals of the abutting struts (orange wireframe, continuing into the remainder of the structure).

References

- 1 Watson JD, Crick FHC, A structure for deoxyribose nucleic acid *Nature* **171**, 737-738 (1953).
- 2 Franklin RE, Gosling RG, Molecular configuration in sodium thymonucleate *Nature* **171**, 738–740 (1953).
- 3 Wilkins MHF, Stokes AR, Wilson HR, Molecular structure of deoxyribose nucleic acids *Nature* **171**, 740–741 (1953).
- 4 Bryan TM, G-quadruplexes at telomeres: friend or foe? *Molecules* **25**, 3686 (2020).
- 5 Seeman NC, Sleiman HF, DNA nanotechnology. *Nature Reviews, Materials* **3**, 17068 (2018).
- 6 Ke Y, Castro C, Choi J, Structural DNA Nanotechnology: Artificial Nanostructures for Biomedical Research. *Annual Review of Biomedical Engineering* **20**, 375-401 (2018).
DOI: 10.1146/annurev-bioeng-062117-120904
- 7 Ge Z, Gu H, Li Q, Fan C, Concept and development of framework nucleic acids. *J. Am. Chem. Soc.* **140**, 17808–17819 (2018).
- 8 Nakata, M Zanchetta, G Chapman, BD Jones, CD Cross, JO Pindak, R Bellini, T & Clark, NA End-to-end stacking and liquid crystal condensation of 6 to 20 base pair DNA duplexes *Science* **318**, 1276–1279 (2007).
- 9 Zanchetta, G Bellini, T Nakata, M & Clark, NA Physical polymerization and liquid crystallization of RNA oligomers *J Am Chem Soc* **130**, 12864–12865 (2008).
- 10 Zanchetta, G Nakata, M, Buscaglia, M Clark, NA & Bellini, T Liquid crystal ordering of DNA and RNA oligomers with partially overlapping sequences *J Phys Condens Matter* **20**, 494214 (2008).
- 11 Bellini, T Zanchetta, G Fraccia, T P Cerbino, R Tsai, E Smith, GP Moran, MJ Walba, DM & Clark, NA Liquid crystal self-assembly of random-sequence DNA oligomers *Proc Natl Acad Sci* **109**, 1110–1115 (2012).
- 12 Zanchetta, G Nakata, M Buscaglia, M Bellini, T & Clark, NA Phase separation and liquid crystallization of complementary sequences in mixtures of nanoDNA oligomers *Proc Natl Acad Sci* **105**, 1111–1117 (2008).
- 13 Fraccia, TP Smith, GP Zanchetta, G, Paraboschi, E Yi, Y Walba, DM Dieci, G Clark, NA & Bellini, T Abiotic ligation of DNA oligomers templated by their liquid crystal ordering *Nat Comm* **6**, 6424 (2015).
- 14 Fraccia, TP Smith, GP Bethge, L Zanchetta, G Nava, G Klussman, S Clark, NA & Bellini, T Liquid crystal ordering and isotropic gelation in solutions of four-base-long DNA oligomers *ACS Nano* **10**, 8508-8516 (2016).
- 15 Fraccia, TP Smith, GP Zanchetta, G, Paraboschi, E Yi, Y Walba, DM Dieci, G Clark, NA &

Bellini, T Abiotic ligation of DNA oligomers templated by their liquid crystal ordering *Nat Comm* **6**, 6424 (2015).

16 Todisco M, Fraccia TP, Smith GP, Corno A, Bethge L, Klussmann S, Paraboschi EM, Asselta R, Colombo D, Zanchetta G, Clark NA, Bellini T, Nonenzymatic Polymerization into Long Linear RNA Templated by Liquid Crystal Self-Assembly *ACS Nano* **12**, 9750-9762 (2018).

DOI:10.1021/acsnano.8b05821

17 Smith GP, Fraccia TP, Todisco M, Zanchetta G, Zhu C, Hayden E, Bellini T, Clark NA, Backbone-free duplex-stacked monomer nucleic acids exhibiting Watson-Crick selectivity *Proc Natl Acad Sci* **115**, 7658-7664 (2018). DOI: 10.1073/pnas.1721369115 PNAS

18 L. Lucchetti, TP Fraccia, G Nava, T Turiv, F Ciciulla, L Bethge, S. Klussmann, OD Lavrentovich, T. Bellini, Elasticity and Viscosity of DNA Liquid Crystals. *ACS Macro Lett.* **9**, 1034-1039 (2020). DOI: 10.1021/acsmacrolett.0c00394

19 JM Berg JM, Tymoczko JL, Gatto Jr. GJ, Stryer L. (2015) *Biochemistry, 8th Edition* (W.H. Freeman, New York).

20 Livolant, F Levelut, AM Doucet, J & Benoit, JP The highly concentrated liquid-crystalline phase of DNA is columnar hexagonal *Nature* **339**, 724-726 (1989).

21 Livolant, F Leforestier, A Condensed phases of DNA: structures and phase transitions *Prog. Polym. Sci.* **21**, 1115-1164 (1996).

22 Maiti PK, Lansac Y, Glaser MA, Clark NA, Isodesmic self-assembly in lyotropic chromonic systems *Liquid Crystals* **29**, 619-626 (2002).

23 Bohle AM, Holyst R, Vilgis, T, Polydispersity and ordered phases in solutions of rodlike macromolecules *Physical Review Letters* **76**, 396-1399 (1996).

24 Wing R, Drew H, Takano T, Broka C, Tanaka S, Itakura K, Dickerson, RE, Crystal structure analysis of a complete turn of B-DNA. *Nature* **287**, 755-758 (1980). DOI: 10.1038/287755a0

25 Franklin R, Gosling R, Molecular configuration in sodium thymonucleate. *Nature* **171**, 740-741 (1953).

26 Podgornik R, Strey HH, Parsegian VA, Colloidal DNA *Curr. Opin. Colloid Interface Sci.* **3**, 534-539 (1998).

27 Strey, HH, Parsegian, VA Podgornik, R, Equation of state for polymer liquid crystals: theory and experiment *Phys Rev E* **59**, 999-1008 (1999).

28 Smith GP, Liquid crystals formed by short DNA oligomers and the origin of life, Ph.D. Thesis, University of Colorado, Boulder (2018).

29 Lyubartsev AP, Nordenskiöld L, Monte Carlo Simulation Study of Ion Distribution and

- Osmotic Pressure in Hexagonally Oriented DNA. *J. Phys. Chem.* **99**, 10373-10382 (1995).
- 30 Davis JT, G-quartets 40 years later: from 5'-GMP to molecular biology and supramolecular chemistry *Angew. Chem. Int. Ed.* **43**, 668-698 (2004).
- 31 SantaLucia J, Hicks D, The Thermodynamics of DNA Structural Motifs. *Annu. Rev. Biophys. Biomol. Struct.* **33**, 415– (440 2004).
- 32 Jana j, Weisz K, Thermodynamic Stability of G-Quadruplexes: Impact of Sequence and Environment. *ChemBioChem* **22**, 2848-2856 (2021). DOI: 10.1002/cbic.202100127
- 33 Kumar N, Maiti S, A thermodynamic overview of naturally occurring intramolecular DNA quadruplexes, *Nucleic Acids Research* **36**, 5610-5622 (2008). DOI: 10.1093/nar/gkn543
- 34 Zanchetta G, Giavazzi F, Michi Nakata M, Buscaglia M, Cerbino R, Clark NA, and Bellini T, Right-handed double-helix ultrashort DNA yields chiral nematic phases with both right- and left-handed director twist. *Proc Natl Acad Sci* **107** 17497-17502 (2010). DOI: 10.1073/pnas.1011199107
- 35 Rossi M, Zanchetta G, Klusmann S, Clark NA, Tommaso Bellini T, Propagation of Chirality in Mixtures of Natural and Enantiomeric DNA Oligomers. *Phys. Rev. Letters* **110**, 107801 (2013). DOI: 10.1103/PhysRevLett.110.107801
- 36 Nava G, Carducci F, Itri R, Yoneda JS, Bellini T, Mariani P, Quadruplex knots as network nodes: nano-partitioning of guanosine derivatives in supramolecular hydrogels. *Soft Matter* **15**, 2315-2318 (2019). DOI: 10.1039/c8sm02616e

SUPPLEMENTARY INFORMATION

A self-assembled periodic nanoporous framework in aqueous solutions of the DNA tetramer GCCG

Gregory P. Smith^a, Tommaso P. Fraccia^{b,c},
Chenhui Zhu^d, Tommaso Bellini^{b,2}, Noel A. Clark^{a,2}

^aDepartment of Physics and Soft Materials Research Center, University of Colorado, Boulder, CO, 80309-0390

^bDipartimento di Biotecnologie Mediche e Medicina Traslazionale, Università degli Studi di Milano, via Fratelli Cervi 93, I-20090 Segrate (MI), Italy

^cInstitut Pierre-Gilles de Gennes, Chimie Biologie et Innovation, ESPCI Paris, PSL University, CNRS, 6 rue Jean Calvin, 75005, Paris, France

^dAdvanced Light Source, Lawrence Berkeley National Laboratory, Berkeley, CA 94720 USA

²To whom correspondence may be addressed: noel.clark@colorado.edu

Abstract

The collective behavior of the shortest DNA oligomers in high concentration aqueous solutions is an unexplored frontier of DNA science and technology. Here we broaden the realm of DNA nanoscience by demonstrating that single-component aqueous solutions of the DNA 4-base oligomer GCCG can spontaneously organize into three-dimensional (3D) periodic mesoscale frameworks. This oligomer can form B-type double helices by Watson-Crick (WC) pairing, into tiled brickwork-like duplex strands, which arrange into mutually parallel arrays and form the nematic and columnar liquid crystal phases, as is typical for long WC chains. However, at DNA concentrations above 400mg/mL, these solutions nucleate and grow an additional mesoscale framework phase, comprising a periodic network on a three dimensional body-centered cubic (BCC) lattice. This lattice is an array of nodes (valence-8, each formed by a pair of quadruplexes of GCCG terminal Gs), connected with a separation of 6.6 nm by struts (6-GCCG-long WC duplexes). This 3D-ordered DNA framework is of low density (DNA volume fraction ~0.2), but, due to its 3D crystal structure, is osmotically incompressible over its phase range. Atomistic simulations confirm the stability of such structures, which promise to form the basis of novel

families of simply and inexpensively made nanoscale frameworks for templating and selection applications.

Table of Contents

Section S1 – Materials and methods	3
S1.1 – Synthesis of GCCG DNA.....	3
S1.2 – Optical microscopy.....	3
S1.3 – X-ray diffraction (XRD) of GCCG samples.....	4
S1.4 – Molecular dynamics simulation of GCCG structures.....	5
Section S2 – GCCG &, ATTAp optical textures & phase diagram from [1] (Figs. S1,S2)	9
Section S3 – Atomistic simulation configurations	11
S3.1 – Simulation to 20 ns (Figs S3 - S8).....	11
S3.2 – Simulation to 150 ns (Fig. S9).....	17
Section S4 – Atomistic simulation to 150ns videos	18
Section S5 – Pitch of the WC double helices in the struts (Fig S10)	20
Section S6 – Osmotic pressure in GCCG solutions (Fig S11)	21
Section S7 – Optical textures of GCCG (Figs S12,S13)	23
Supplement references	26

Section S1 – Materials and methods

S1.1 – Synthesis of GCCG DNA – GCCG oligomer DNA was custom synthesized as previously described in Ref. [1]. In short, the DNA was synthesized on an Akta Oligopilot 100 fixed volume packed bed synthesizer by the Caruthers synthetic method at a scale of 243 μmols . DNA obtained by this process was deprotected in ammonium hydroxide, filtered and purified by isopropanol precipitation to obtain liquid crystal forming product which was then typically lyophilized.

Synthetic processing of this DNA sample differed from other oligomer DNAs we've produced previously because we discovered that the liquid crystal forming behavior of this material is quite highly sensitive to counterion identity and concentration. To regulate counterions, we dialyzed the DNA as necessary against fixed salt concentrations of 50 mM to 500 mM in 500 MWCO dialysis micro devices. Dialysis was typically undertaken on two or three 1L changes overnight. The BCC phase has appeared in samples where the salt, NaCl, is particularly regulated to ~ 100 mM and glassy isotropic phases tend to dominate in samples with NaCl regulated 300 mM or higher during dialysis. Samples without careful regulation of salt content have been devoid of BCC phase in favor of apparent isotropic gels. If Li^+ is used instead of Na^+ , the observed LC phase behavior is almost entirely suppressed.

S1.2 – Optical microscopy – DNA samples were prepared in eppendorf tubes by adding water to set weights of powdered DNA. Water was centrifuged down the container wall by microfuge to combine the DNA with water and then several short incubations were carried out at 85°C to mix them. For this sample, LC was transferred from the eppendorf to a glass slide by a micropipettor whenever possible, but the unusually high viscosity of the GCCG mixture sometimes necessitated use of a micro-spatula instead. LC placed on a glass slide was covered by a glass coverslip and the void filled with mineral oil to restrict evaporation. The optical path length in these samples was not constrained.

Optical microscopy was carried out in an Instec hotstage equipped with a thermoelectric coupler using a Nikon microscope. A linear polarizer was set on the light source and a second, the analyzer, was equipped after the objective. These were typically crossed to render isotropic sample as a dark field where birefringent LC domains appear in bright colors. Photography was carried out in situ on the microscope by use of an Olympus digital camera on a secondary optical path. We calibrated the size of the microscope field using pictures of a microscopic reticle at the different objective powers. Typically, the microscope stage was carefully centered to enable examination of extinction brushes by rotating the stage. We examined the phase diagram of GCCG in two dimensions, noting the morphology of microscopic LC textures at set water-DNA concentrations and performing temperature ramps at those concentrations. It is noteworthy that glass slide cells become unstable at higher temperatures when water vapor starts escaping through the mineral oil seal. We have remedied this in turns by addition of slide layers in the cell

which restrict the localization of the sample by surface tension and by use of flame sealed glass capillaries in place of open cells.

S1.3 – X-ray diffraction (XRD) – We contained GCCG samples stably in glass capillaries prior to subjecting them to synchrotron X-ray diffraction. The capillaries used were cylindrical capillaries made of borosilicate glass 2mm in diameter. We selected these capillaries in particular because they are robust and withstand centrifugation, unlike thinner quartz capillaries typically used for XRD experiments which are not durable in the centrifuge. Solid GCCG powder was packed gently into the entry of the capillary, then centrifuged to the bottom by ultra-centrifuge at 22,000rpm in a special holder floating on high density fluorinated oil inside the centrifuge tube. Water was then added to the powder, again by centrifuge. Afterward, the capillary was sealed by the flame of an oxygen-propane torch and the concentration equilibrated by repeatedly cycling the temperature between room temp and 90° C. If concentration is uniform, the entire capillary should uniformly transition between LC phases at a very specific temperature and it should transition nearly simultaneously. Concentration was determined by tracking the masses of the water and DNA added and supported by examining the apparent phases in the capillary. Because we chose to use borosilicate glass capillaries in an X-ray experiment it was important to check the diffraction of empty samples to look for diffraction of the container, which was never seen. It is also noteworthy that this form of sample is most suitable in a synchrotron X-ray source because sources with lower fluence do not transmit very well through this kind of glass. Additionally, these capillaries are challenging to examine by optical microscopy due to their cylindrical cross section; we observed them by an index matching scheme looking through a jig containing oil to correct for refraction of the optical paths across the interfaces.

WAXS at 0.1 to 3.0 Å⁻¹ was carried out on GCCG samples at ALS beamline 7.3.3 with an X-ray wavelength of 1.24 Å. Scattering was visualized by use of a Pilatus 2M detector on the beamline [14]. We calibrated the scattering by collecting shots from Silver Behenate, which has well characterized diffraction peaks, at the same sample to detector distance. The sample temperature was regulated during the diffraction experiment by use of an Instec microscopic hotstage that was connected to a water circulator for active cooling. In addition to examining a sequence of different concentrations to fully view that dimension of the phase diagram, we performed a series of 0.1 to 0.5 second exposures on the sample while increasing the hotstage from room temperature up through the isotropic phase transition at about 90°C. An additional observation was then made by turning off the hotstage heating and circulating cool water through the stage to rapidly crash back to room temperature and taking X-ray exposures while the temperature dropped.

We processed the data from the X-ray observations using the Nika software tool on Igor Pro [15]. Subsequent data manipulation for presentation purposes was carried out on Origin Pro and Microsoft Excel. Some spacings in the 2D data sets were also examined using ImageJ [16].

S1.4 – Molecular dynamics simulation of GCCG structures – We produced an MD simulation of the GCCG L2 eight-armed star node using the Gromacs-2022 and -2023 MD simulation systems [17]. To avoid the complexity of attempting to produce our own force field, we chose to employ the AMBER99SD-ILDN force field packaged with Gromacs. We picked Amber in particular because of its history in the field of DNA MD simulation. Because the work-flow for Gromacs is well domesticated for translating targets from Protein Data Bank information into MD simulations, we needed to enter this workflow by developing our own means of setting up the target GCCG structure since no full crystal structure of the proposed node actually exists. We failed initially with AMBERTools and sought instead to produce our own rudimentary software using Microsoft Visual Studio 2022 and C++ to fabricate the starting molecular geometry for the simulation.

We used the 4c64 PDB structure of Dickerson Dodecamer as a model for B-form duplex DNA. From this, we developed a series of linear transformations extracted from the coordinates of the crystal structure to project one DNA base-pair through a set of consistent rotations and translations in order to produce an acceptable generalized B-form DNA duplex. We expanded on this and tailored our software to convert any base-pair sequence into a B-form duplex of any desired length, including choice single-stranded and double-stranded regions and with backbone modifications to enable selected strand breaks terminating on 3' and 5' hydroxyls. This enabled us to develop a contiguous B-form duplex with antiparallel backbones composed of 6 discrete, base-paired GCCG oligomers. We chose arbitrarily to leave the overhangs as 5' single-stranded GC- regions as opposed to 3' overhangs or some mix of 5' and 3' between struts. Within this model, as with the analogous crystal structure, hydrogen atom coordinates were omitted and we planned to rely on Gromacs software filling in these atoms. The program for producing this structure was written as a simple command line program.

The guanine rich node we decided to simulate as a pair of stacked G-quartet structures, creating a bare minimum G-quadruplex. To this end, we used Gaussian 16 [18] on the University of Colorado Summit supercomputer to refine the geometry of a single guanine quartet liganded around a sodium atom. Within this quartet, the guanine was reduced to omit sugars and retain only four copies of the bare minimum nitrogenous base by itself. We refined a DFT geometry using APFD/6-311++G(d,p) and a polarizable continuum model to simulate solvation in water; APFD was chosen because it contains an empirical dispersion correction [19] and we wanted to try to optimize as if we were producing realistic hydrogen bonding between the guanines.

We programmatically manipulated the simulated G-quartet coordinates to produce the desired quartet stack. This stack was further manipulated to integrate it into the center of the L2 node model starting geometry, surrounding it by a collection of eight GCCG struts that replace a terminal 5' unpaired guanine with the G-quadruplex guanines, incorporating all the atoms so that they were present in the appropriate oligomer tabulation as would be necessary to facilitate

the MD simulation topology. The program for producing these manipulations is analogous to a script and accessed through Microsoft Visual Studio; an interface was not created for the program.

In the meantime, we used a single GCCG oligomer which we ran through the Gromacs `pdb2gro` utility in order to produce a topology reflective of the single intact molecule. Additional molecules were added to illustrate the L2 node structure by simply adding an appropriate number of GCCG units to the topology, as long as expected numbers occur in the right order in the geometry file. With this we created a Gromacs `*.gro` geometry file containing 48 GCCG oligomers with 125 atoms each, including hydrogens, all appropriately assigned from the same molecular topology. This coordinate system was then further manipulated using `gmx solvate` to add water molecules and `gmx genion` to include sodium counterions sufficient to negate the charge of the DNA system. Two of these sodium atoms were placed into the core of the G-quadruplex at the Gaussian 16 determined sodium positions.

The resulting starting system contained 48 GCCG oligomers, 13990 spce water molecules and 144 sodium atoms. This gives a total of 48,114 centers in a box with periodic x , y , z boundaries the size of 8.4 nm \times 8.4 nm \times 6.9 nm. It is noteworthy that MD simulations of DNA liquid crystals are expensive because of their lyotropic nature; the majority of simulated centers here are water and it can be challenging to appropriately scale the box a priori to match a desired concentration. The simulation of 48,114 centers stretched our resources and was too small a simulation in terms of volume to assure that the gigantic node was not interacting directly with itself across the periodic boundaries, though this concern is somewhat mitigated by the sheer volume of water in the computation. Our initial desire was to genuinely create the node by linking G-quartets at the corners of the box across periodic boundaries, but this proved too difficult to plan with our current tools.

The MD simulations were carried out using Gromacs-2022 and Gromacs-2023 [17] on a GPU partition node of the University of Colorado Summit, and later Alpine, research computing clusters. The simulation was carried out in three stages using the Amber force field. The initial geometry was first relaxed by energy minimization using steepest decent to achieve a geometry relaxed away from the initial starting state which contained some small bond geometry pathologies carried over from the creation of the model. The geometry was then run through a 100 ps NVT simulation step at 293 K temperature with the DNA heavy atoms restrained in place. NVT phase was run twice, for a total of 200 ps. We then switched to an NPT phase, again holding temperature at 20° C and performing pressure coupling on an isotropic scheme (all walls coupled) with pressure referencing set to 1 bar and compression controlled by the C-rescale Berendsen-like barostat and ran for 1 ns with the position restraints released.

Simulations were made in two separate efforts; the first leading to only 20 ns of simulation time and the second to 150 ns on newer supercomputing infrastructure. We switched to this longer

simulation time based on a nearly independent observation that our MD simulations tended to achieve real pressure and behavioral equilibrium after at least 100 ns of run time.

A large refinement was also made between the simulation trials. In the early 20 ns trial, the size of the simulation box was larger than the size of the BCC lattice unit cell by an appreciable amount, while the sodium concentration was confined to render the simulation net neutral in charge, meaning that the counterion concentration was lower than would be present in the real BCC lattice structure. Additionally, the struts in the cell were unrestrained to a lattice and free to move throughout the volume of the cell. As such, this creates a situation where the concentration of the LC is low, perhaps destabilizing the structure as a result. For the second trial, we recreated the topology to include three types of GCCG oligomer unit; a topology for a tail oligomer that would be single-stranded at the strut terminal, a topology for a body oligomer which would be fully W-C paired at the beginning of the simulation and a core topology which is single-stranded into the G-quartet core. The core type topology was enabled to contain position restraints with a harmonic force constant of $\sim 5.5 \text{ kJ}/(\text{mol}\cdot\text{nm}^2)$ on the atoms of the guanine participating in the G-quartet node at some position of choice, with each core type topology identified uniquely by strut. The body type topologies contained no specific restraints. The tail type topologies each contained a $\sim 5.5 \text{ kJ}/(\text{mol}\cdot\text{nm}^2)$ restraint on the O6 oxygen of the guanine aromatic base at the far terminal of the strut. These restraints allowed for pinning the struts in place either at the core, or at the single-stranded tails at any desired position in the simulation cell. The core restraints were used to immobilize the G-quartet node during segments of the simulation that were involved with start-up and early equilibration to try to mitigate the effects of large, unrealistic forces that might destroy the node prior to reaching a stable phase of the simulation. The tail restraints were used throughout the simulation to pin the tails of the struts onto a cubic footprint the same size as the BCC fundamental lattice cell, as determined by XRD, thus artificially restraining the concentration of the DNA to remain roughly at the value and distribution present in the BCC lattice. Sodium ions were fully unrestrained, leaving them perhaps artificially low in concentration, but we believe not significantly given that they tend to explore space near the DNA based on their complementary charge. During the simulation, restraint positions were calculated relative to the center of mass of the DNA configuration, as determined by Gromacs.

During the running of the more modern 150 ns simulation, the core and tail restraints were imposed during NVT and initial NPT phases of the simulation. The barostat was switched to Parinello-Rahman after the NPT and the restraints on the core were released, leaving only the tail-terminal restraints.

We performed analysis of Gromacs generated simulation trajectory files using custom software written in C++17 standard on Microsoft Visual Studio 2022 IDE. This software, made freestanding as a Win32 app, is able to extract selected atom positions directly from binary Gromacs *.xtc trajectory files and facilitate select analysis by generating relative coordinates from these

positions. Data extracted from the trajectory in this way was further processed using Microsoft Excel and Origin Pro. The authors wish to note that this sort of simulation is made very expensive in time because liquid crystal simulation is not directly supported by the Gromacs native workflow; building up software to create starting geometries readable by Gromacs and then building up software to extract data from trajectories which may be uninteresting to the bulk of Gromacs users was prodigiously time consuming and rate limiting.

Section S2 – 5'-GCCGp-3' & 5'-ATTAp-3' optical textures & phase diagram from [1]

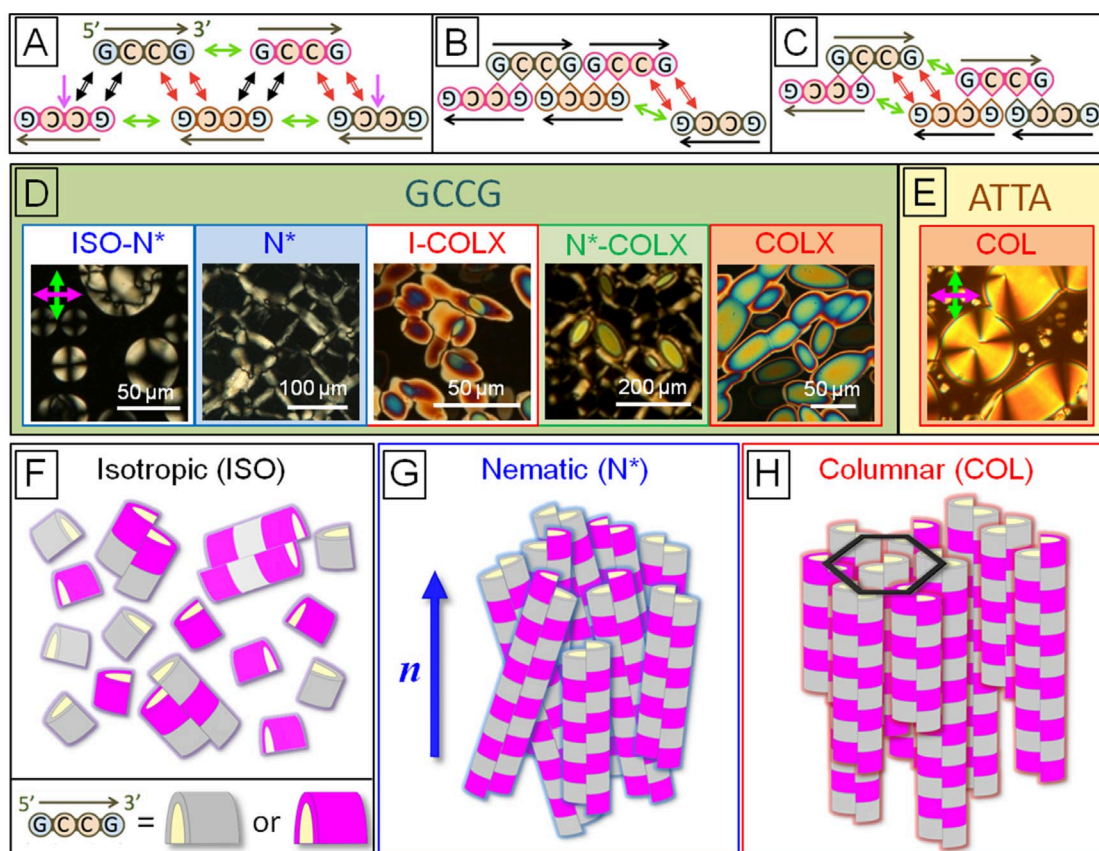


Figure S1: Modes of assembly of the 4mers 5' -GCCGp-3' and 5' -ATTAp-3' . (A) Pairing and stacking interactions at play in the stability of the GCCG aggregates: Watson-Crick GC/CG quartets (black arrows) and CG/GC quartets (red arrows), coaxial stacking (green arrows), dangling end stacking (between the bases as marked by pink arrows). (B, C) Interactions at play between an aggregate and a monomer (B) and between two aggregates (C). (D, E) Pictures by polarized transmission optical microscopy of thin cells of GCCG (D) and ATTA (E) at T = 10 °C and distinct concentrations [from left to right $c_{DNA} = 650$ mg/mL, $c_{DNA} = 260$ mg/mL, $c_{DNA} = 365$ mg/mL, $c_{DNA} = 450$ mg/mL, $c_{DNA} = 500$ mg/mL and T = 25 °C, $c_{DNA} = 570$ mg/mL]. (F-H) Sketches of the self-assembly of DNA 4mers, represented by semicylinders with alternate gray and violet colors to appreciate their binding, in the different phases: isotropic phase formed by single strands and short chains (F), chiral nematic (N*) LC phase in which longer chains are orientationally ordered (G), and columnar (COL) LC phase in which parallel columns free to slide past each other form an hexagonal 2D lattice. (H). Structure of COLX phase. From Ref. [1]. Reprinted with permission.

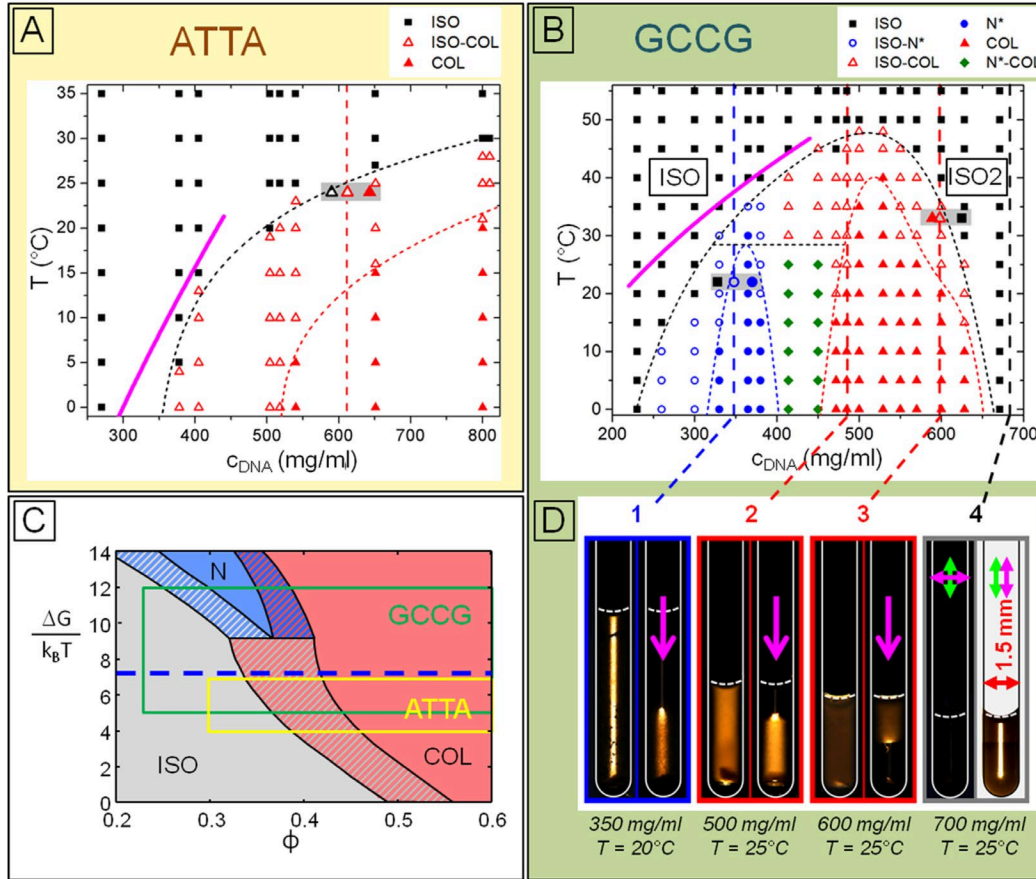


Figure S2: Phase diagram of 5' -GCCGp-3'. (A, B) c_{DNA} - T phase diagram for ATTA (A) and for GCCG (B). Symbols indicate: ISO and ISO2 phase (solid black squares), ISO-N* coexistence (empty blue circles), N* phase (solid blue circles), ISO-COL and ISO-COLX coexistence (empty red triangles), N*-COLX coexistence (solid green diamond), COL and COLX phase (solid red triangles). Thin dashed lines guide the eyes to identify the phase boundaries (black, ISO; blue, N*; and red, COL/COLX). Magenta lines mark the ISO side of the ISO-LC phase coexistence according to the model implemented with ΔG_{ATTA} and ΔG_{GCCG} obtained from melting temperature measurements. Vertical lines and 1-4 labels mark the c_{DNA} where capillaries were prepared and investigated. Symbols over a gray shading indicate the c_{DNA} of the two coexisting phases measured after cutting centrifuged capillaries at the meniscus. (C) $\Phi - \Delta G/k_B T$ phase diagram for DNA duplexes with $L/D = 0.5$ from ref 18; solid contours highlight the volume fraction-energy regions investigated in the experimental phase diagrams of ATTA (yellow) and GCCG (green); blue dashed line indicate the experimental $\Delta G_{MIN}/k_B T \approx 7.3$ for the nematic ordering. (D) Pictures of the larger capillary positioned between crossed polarizers before and after centrifugation (magenta arrow) showing ISO-N* (1), ISO-COLX (2), COLX-ISO2 (3), and ISO2 (4) at c_{DNA} and T as indicated. From Ref. [1]. Reprinted with permission.

Section S3 – Atomistic simulation configurations

S3.1 – Atomistic simulation to 20 ns

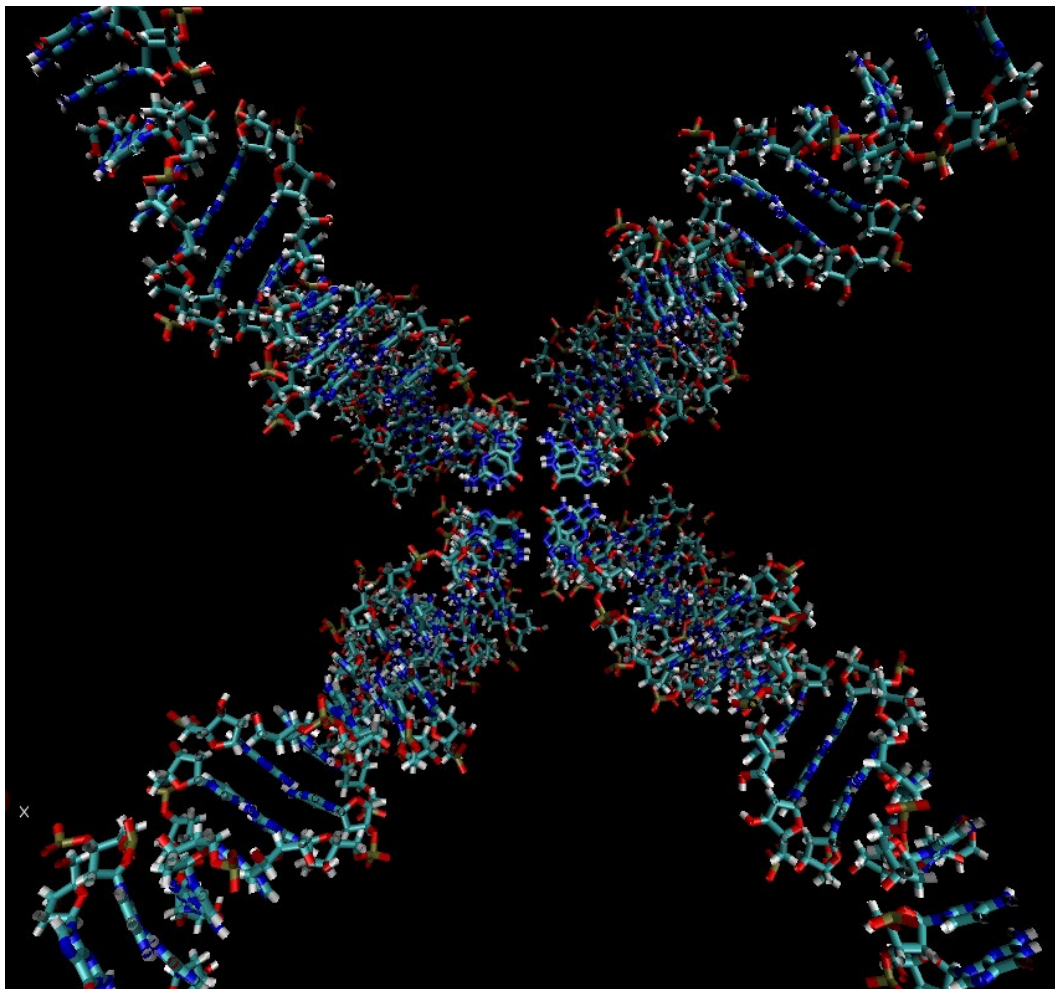


Figure S3: Starting geometry for L2 eight arm star node. Each strut contains six monomeric GCCG oligomers, three running from the overhanging 5' end single-stranded GC at the guanine octet to the 3'-end at the corners of the node and three more antiparallel to make each strut a duplex. Overhangs are uniformly on the 5'-ends of the struts, which may or may not be physically realistic. The structure here was constructed using bespoke computer software written in C++ with Microsoft Visual Studio. Helical geometry parameters were borrowed from a two base-pair section of the X-ray crystal structure for the Drew Dickerson Dodecamer (PDB# 4c64) which was then manipulated to add any choice of base moiety in an acceptable orientation for Watson-Crick base-pairing, then projected by a series of rotations and translations into a helix any number of bases in length and any degree of single- or double-stranded completeness. The g-quartet geometry used was a product of DFT calculations using Gaussian 16. These separate elements were unified using custom software into the model seen in this figure.

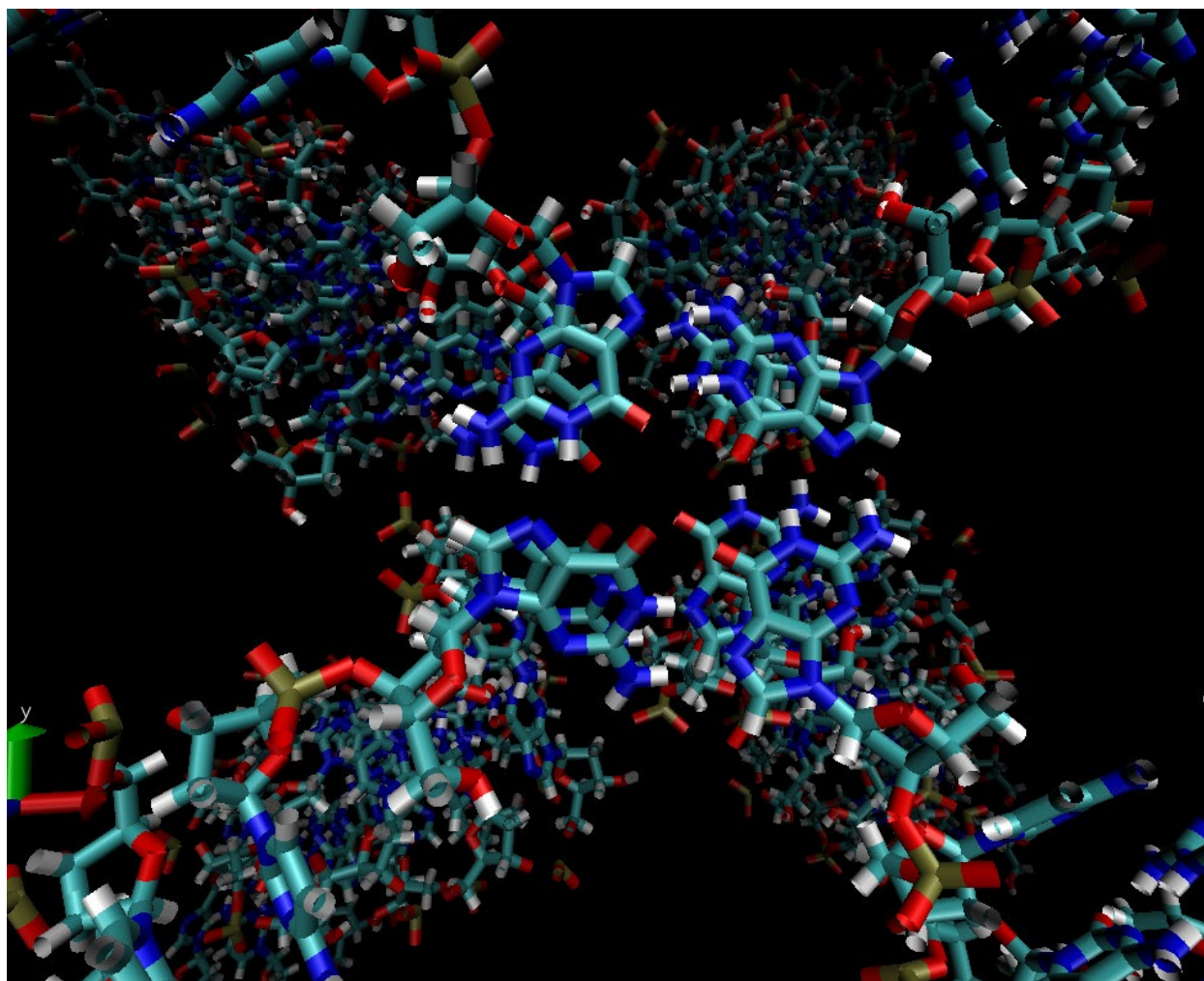


Figure S4: Close-up of the starting state of the stacked g-quartet quadruplex at the core of the L2 eight arm star node. Original G-quartet structure was obtained using Gaussian 16 to model a single Guanine quartet array around a sodium atom using DFT. These structural coordinates were then manipulated to attach them to perviously generated GCCG struts.

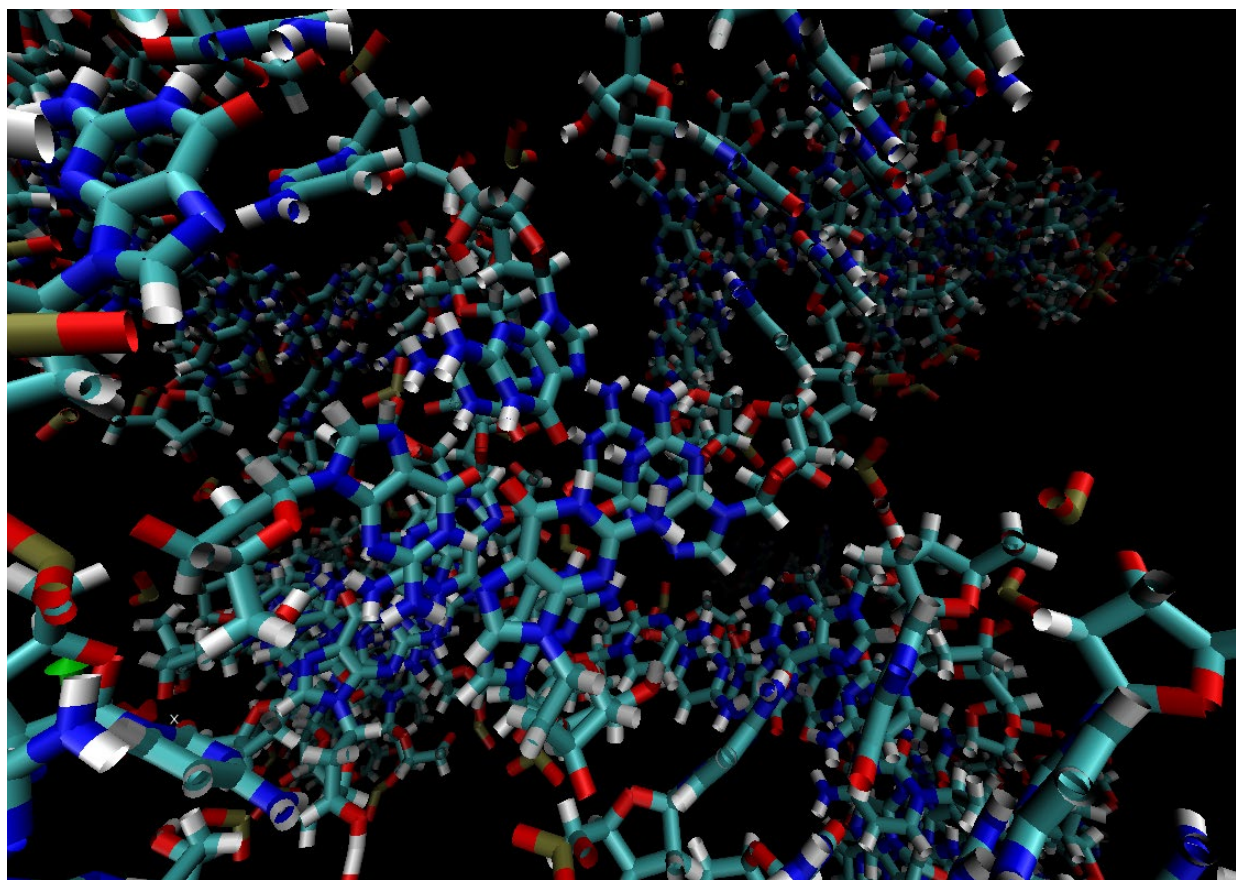


Figure S5: Close-up of G-quartet stack after 20 ns of simulation time in Gromacs using AMBER force field. The node structure is seen to be no longer a fully intact G-quartet pair, but has remained as an interacting, roughly square-shaped mass for the period of the simulation. Because the struts are unrestrained as they would be in a fully translationally symmetric crystal, it is possible that some lateral forces from the spreading out of the struts has helped to disorder the node.

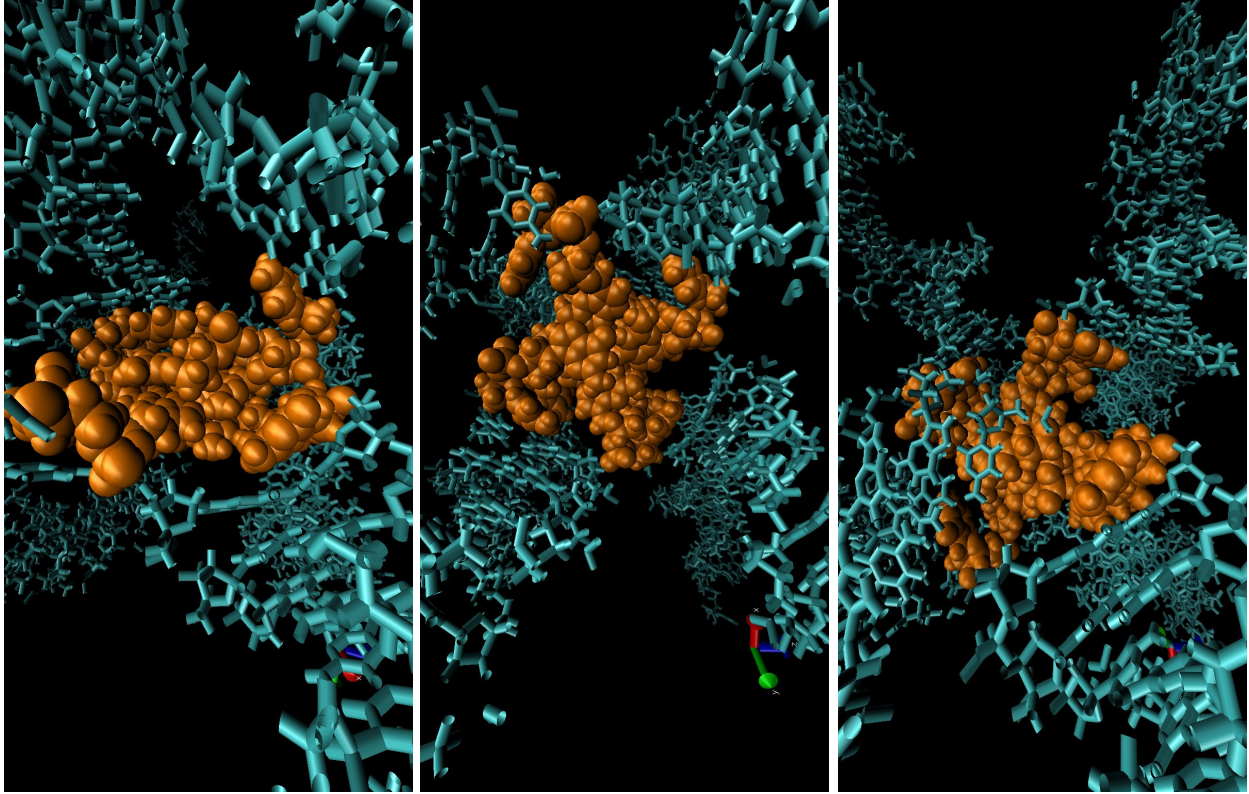


Figure S6: Space-filling image of the G-quartet stack (orange) following 20 ns of simulation time in Gromacs as seen in VMD along the x-axis, and seen from two directions along the z-axis. The node remained associated through the course of the simulation.

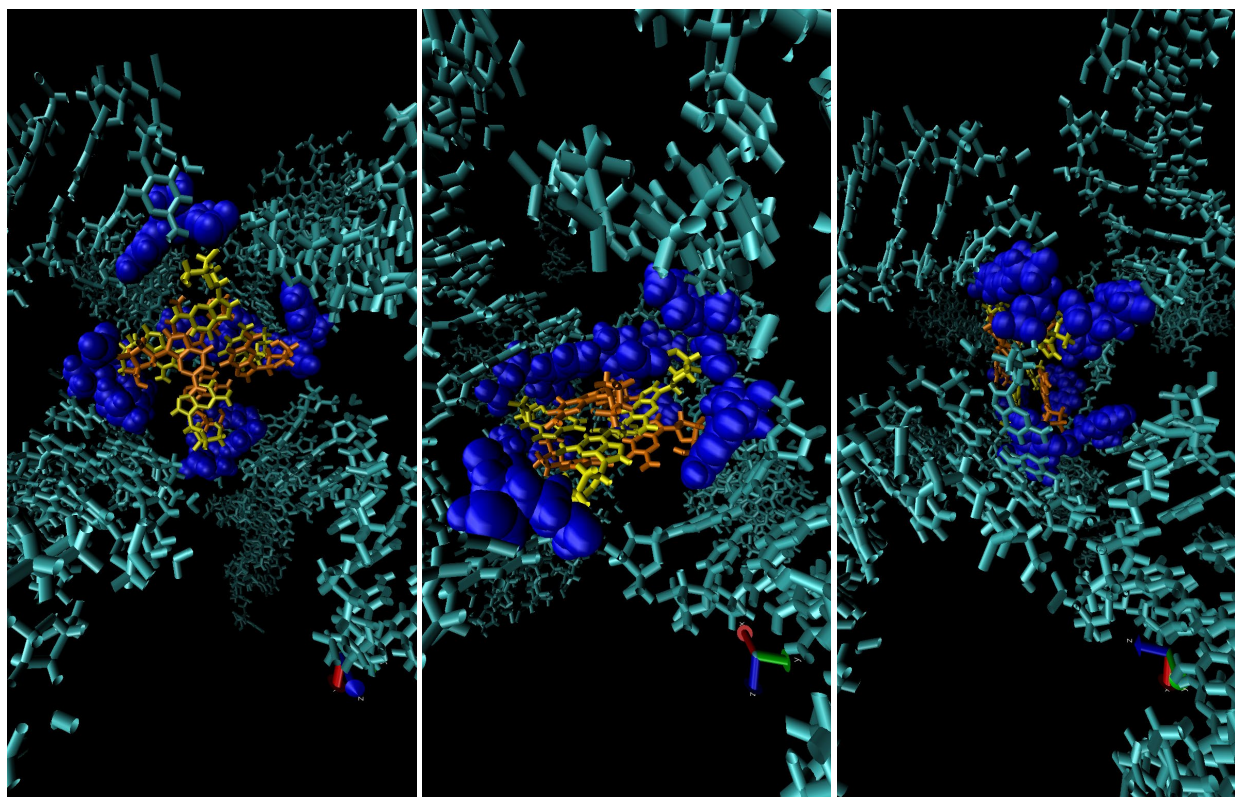


Figure S7: Z-axis, x-axis and y-axis views of the G-quartet node in the L2 eight arm star structure. Fully unpaired cytosine bases in the single stranded GC-overhangs are rendered as blue spacefilling balls. The g-quadruplex guanine stack members are rendered as yellow and orange stick figures.

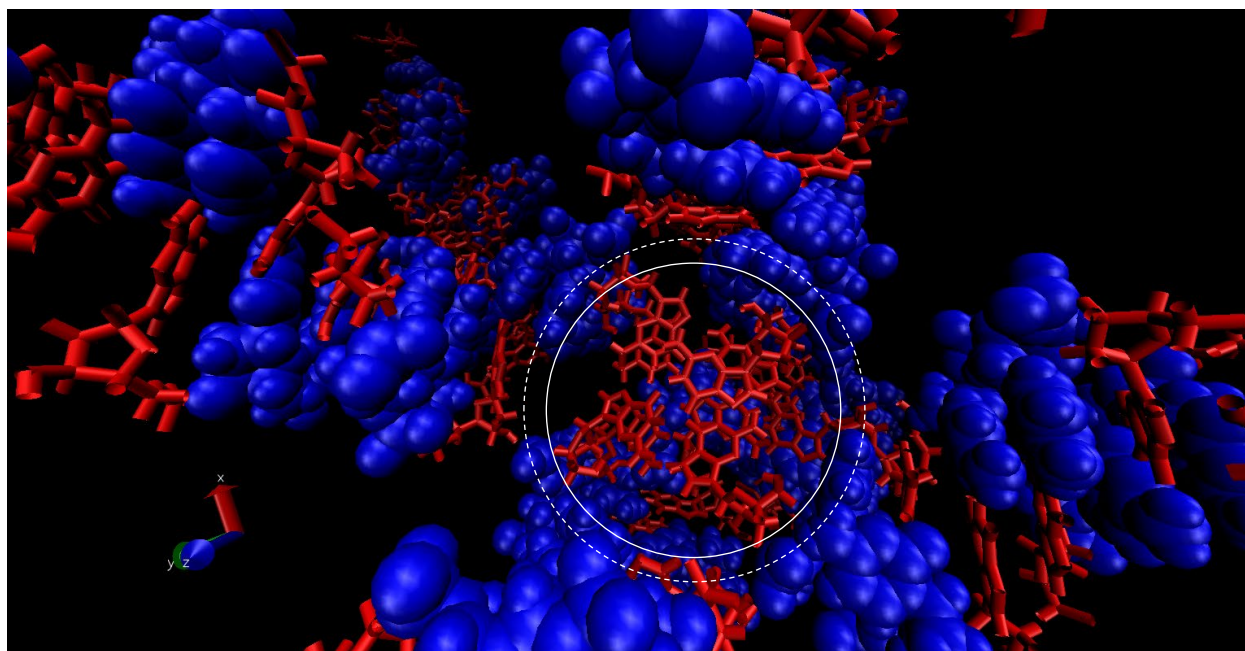


Figure S8: Diagram showing the location of the strut node in a circle with the free cytosines occurring at the dotted line. Guanine residues are red stick figures and cytosine residues and blue spacefilling models.

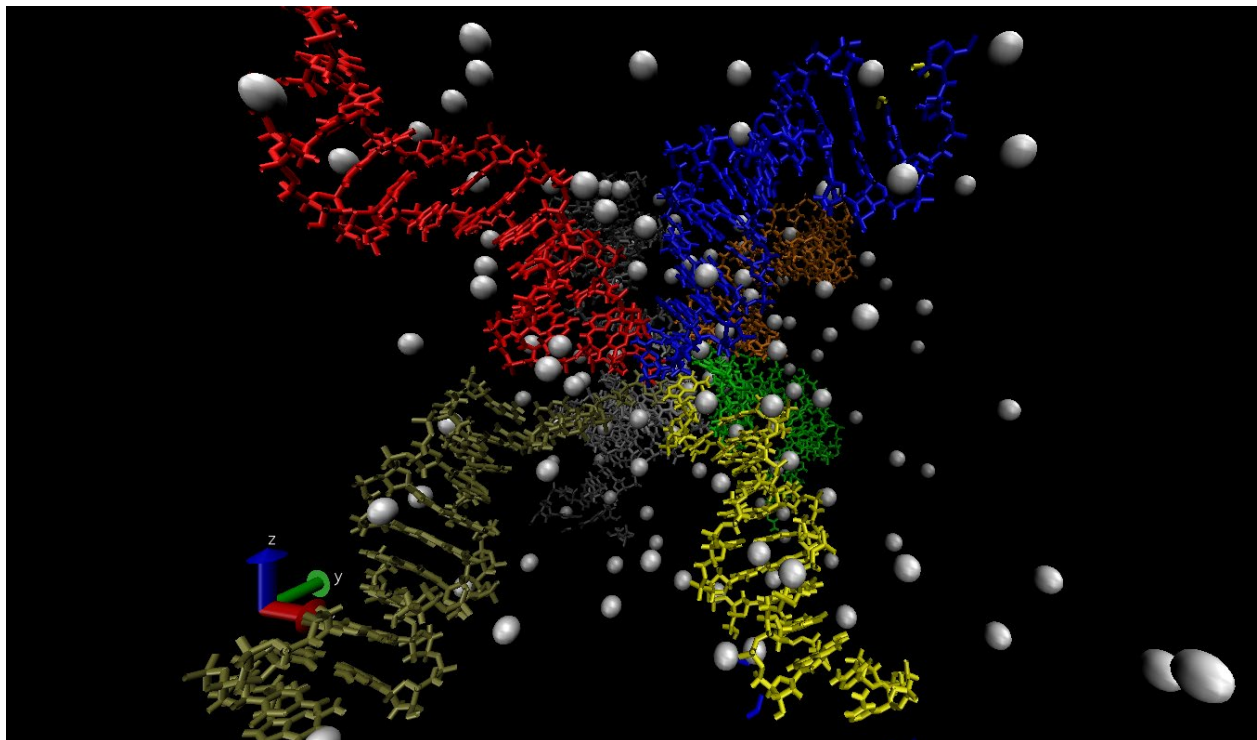


Figure S9: The final configuration of the GCCG L2 node 6 oligomer x 8 strut model following 150 ns of simulation. Each strut is colored for clarity, red, blue, yellow, green, orange, tan, silver and gray. Sodium ions are included as spacefilling gray balls and water molecules are completely omitted to facilitate visibility of the structure. The tips of the struts are restrained via one Guanine O6 oxygen at the points of a cube to simulate restraint to a BCC lattice.

Section S4 – Atomistic simulation to 150ns videos

Video: <GCCG v3 starting state.mp4>

This video is a rotation of the model used for the starting state of the simulation. Each six-oligomer strut is uniquely colored for clarity and the sodium atoms are rendered white and spacefilling so that they can be seen. Water is overwhelmingly present, but has been omitted from the view so that other structures are visible.

Video: <GCCG v3 starting state2.mp4>

This video also shows the starting state for the simulation with the struts uniquely colored. Here, all but two sodium atoms have been omitted; only the two located at the ligand sites in the stack G-quartets remain.

Video: <GCCG v3 xtc15 10 ns 1.mp4>

This video shows the final 10 ns of the 150 ns node structure MD simulation. The frames were captured every 10 ps and are presented without any averaging between frames. The struts are uniquely colored for clarity, the sodium atoms are white spheres and the water molecules are totally omitted.

Video: <GCCG v3 xtc15 10 ns smoothed.mp4>

This video again shows the final 10 ns of MD simulation. Here, the trajectories have been averaged between frames to smooth the motion and make them more visible. Struts are uniquely colored for clarity, sodium atoms are white spheres and water molecules are omitted.

Video: <GCCG v3 xtc15 rotation.mp4>

This video shows a rotation of the final stationary configuration of the MD simulation. Struts, ions and waters are all represented (or not) as the previous videos.

Video: <GCCG v3 trapped Na.mp4>

This video shows the final 10 ns of the simulation with all molecules represented as before. Here, all the extra sodium atoms have been omitted except for the single sodium that is trapped in the core of the node within a G-quartet. Trajectories for the struts are smoothed, while the sodium trajectory is left unaltered.

Video: <GCCG v3 g-quartet.mp4>

This video shows only the persistent g-quartet located at the core of the node, including the four guanines colored red and the sodium ion coordinated with them.

Video: <GCCG v3 full node xtc15 v2.mp4>

This video shows a close-up of the node. The sodium atom is a white sphere and the guanines in the quartet are red. The blue residues are the remaining unpaired guanines and cytosines present in the single stranded overhangs of each strut. Finally, additional visible portions of the struts are rendered in orange wireframe to see that certain cytosines and guanines not present in the single-stranded overhangs have come to participate in the structure of the node.

Section S5 – Pitch of the WC double helices in the struts

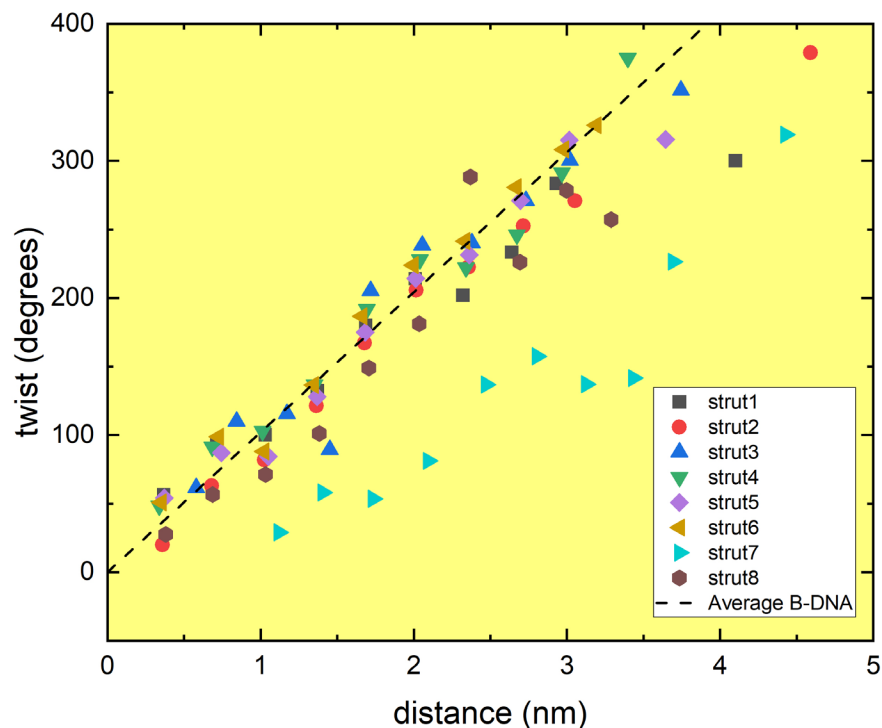


Figure S10: Examination of the pitch of the WC double helix of all the 6-membered GCCG struts during the last 10 ns of a 150 ns simulation, including 1000 frames of trajectory data. Plot data matching the red markers are generated from a series of vectors placed between C4 and H1 in each guanine base in the double-stranded region of the GCCG strut. This marks the position and orientation of each base pair in the strut. The vectors are taken as two-ended since the guanine switches from the parallel to anti-parallel strand every two bases, enabling us to trace the parity of the vector relative to only one of the phosphate backbones in the duplex. Axis label ‘distance’ is the magnitude of separation in nm between the tail of the first base-pair vector and the tail of each guanine bound vector afterward. ‘Helix twist’ is obtained from the dihedral angle between each pair of vectors. The dashed line marks the distance versus twist for typical B-form DNA assuming the base stacking period is 3.39 Å and the number of bases per 360 degrees of helical twist is 10.4. For this simulation segment, the GCCG struts follow the accepted B-form twist and particularly the average slope. The most major deviation, by strut 7, is due to a melting event where the terminal guanine used as the reference base came detached from the continuous run of Watson-Crick paired bases composing the core of the strut and instead associated into the side of the hydrophobic central node without being paired to its complementary cytosine. The resulting gap does not change that the strut still comes close to subtending a slope that is approximately B-form.

Section S6 – Osmotic pressure in GCCG solutions

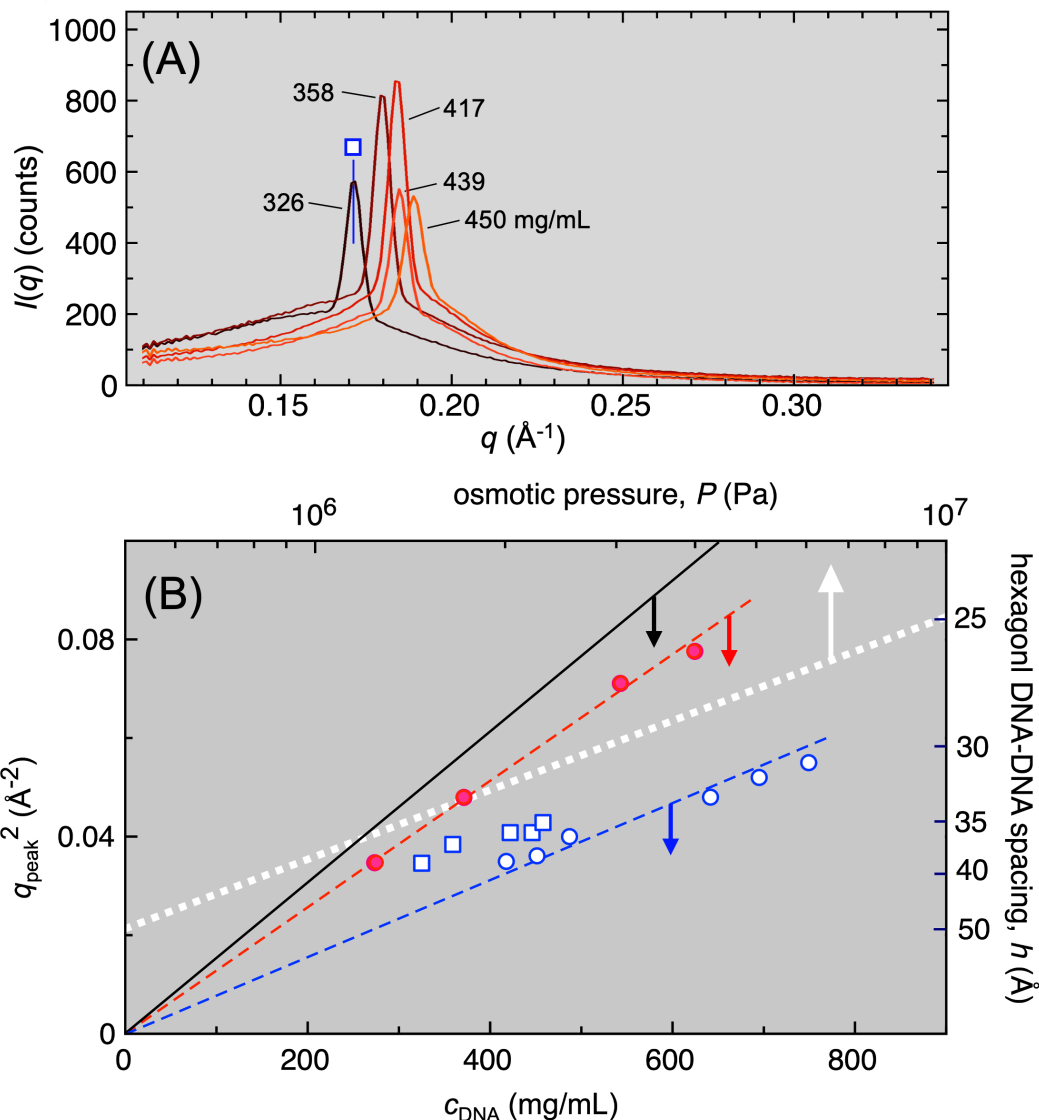


Figure S11: The lack of dependence on solution concentration c_{DNA} of the BCCX in Fig. 6 can be usefully contrasted with that of the NEM and COL phases of GCCG, also visible in Fig. 6. Specifically, Fig. 6 shows that in solutions with coexisting BCCX and COL phase, as concentration c_{DNA} increases, q_{peak} , the position of the diffuse scattering peak near $q_p \sim 0.2 \text{\AA}^{-1}$, indicated in q by the blue '+' s increases, with q_p^2 approximately proportional to c_{DNA} . This behavior is found in long duplex DNA [2,3], complementary dodecamers [4], and shorter oligomers [5]. In long DNA the duplex chains behave as covalently polymerized flexible repulsive rods, which, at higher concentrations, orient mutually parallel and pack into local hexagonal lattices with a lattice parameter (rod-to-rod spacing), $h(c_{\text{DNA}}) = [2/\sqrt{3}]2\pi/q_{\text{peak}}(c_{\text{DNA}})$, that depends on concentration c_{DNA} . This equation is plotted as the solid black line in (A), and should be applicable if it is assumed

that the rods are fixed in length and packed on a defect-free hexagonal lattice, apparently the condition actually approached by long DNA [Error! Bookmark not defined.]. And $N > 12$ oligomers (red points are $N = 12$ data) In the COL phases this hexagonal order is long-ranged [4,6], while in the NEM phases it characterizes the structure of local short-range inter-rod correlations [7]. In the small- N cases the duplex-chain rods are stabilized by end-to-end adhesion of the shorter oligomers [4,8,9]. Small length-wise compressibility of the rods is a reasonable assumption considering the constancy of the spacing, d , of the periodic of base stacking in B-DNA, with $d \approx 3.4 \text{ \AA}$ in systems ranging from concentrated crystalline B-DNA [10,11] to COL LC phases of G-quadruplex four-chain stacks [12]. On the other hand, due to the softness of the entropic and electrostatic repulsions between the rods, $h(c_{\text{DNA}})$ can be continuously reduced to $h(c_{\text{DNA}}) \sim 25 \text{ \AA}$ by osmotic compression [3]. Such a variation can be achieved by controlling either the DNA concentration or the DNA osmotic pressure directly [3,13], the latter showing that h data can be used to read out DNA osmotic pressure, as indicated by the dotted white line in Fig. S11B. Thus, at lower temperatures in the BCCX hatched region, in addition to the BCCX diffraction peaks we observe a broad residual peak in the background near $q \sim 0.2 \text{ \AA}^{-1}$, that indicates coexistence of the NEM or COL with the BCCX and can be used to estimate NA osmotic pressure in added-salt-free, hexagonally ordered DNA [13Error! Bookmark not defined.]. The data in Fig. 11B show that in GCCG solutions there is less osmotic compression at a given c_{DNA} than in long DNA, perhaps a result of disordering the COL phase. However, it is reasonable to assume that the relationship between osmotic pressure and q_{peak} is preserved, since it depends primarily on side-by-side duplex repulsion. If this is the case then the white dotted line in Fig. 9B can be used to obtain osmotic pressure in the GCCG solution, by projecting blue data points horizontally to the white line, and then up to the osmotic pressure scale. The result is an increase to $P \sim 3 \text{ Mpa}$ at the highest concentrations in the BCCX range. Note that the hexagonal DNA-DNA spacing scale on the right corresponds exactly to the q_{peak} scale on the left.

Section S7 – Optical textures of GCCG

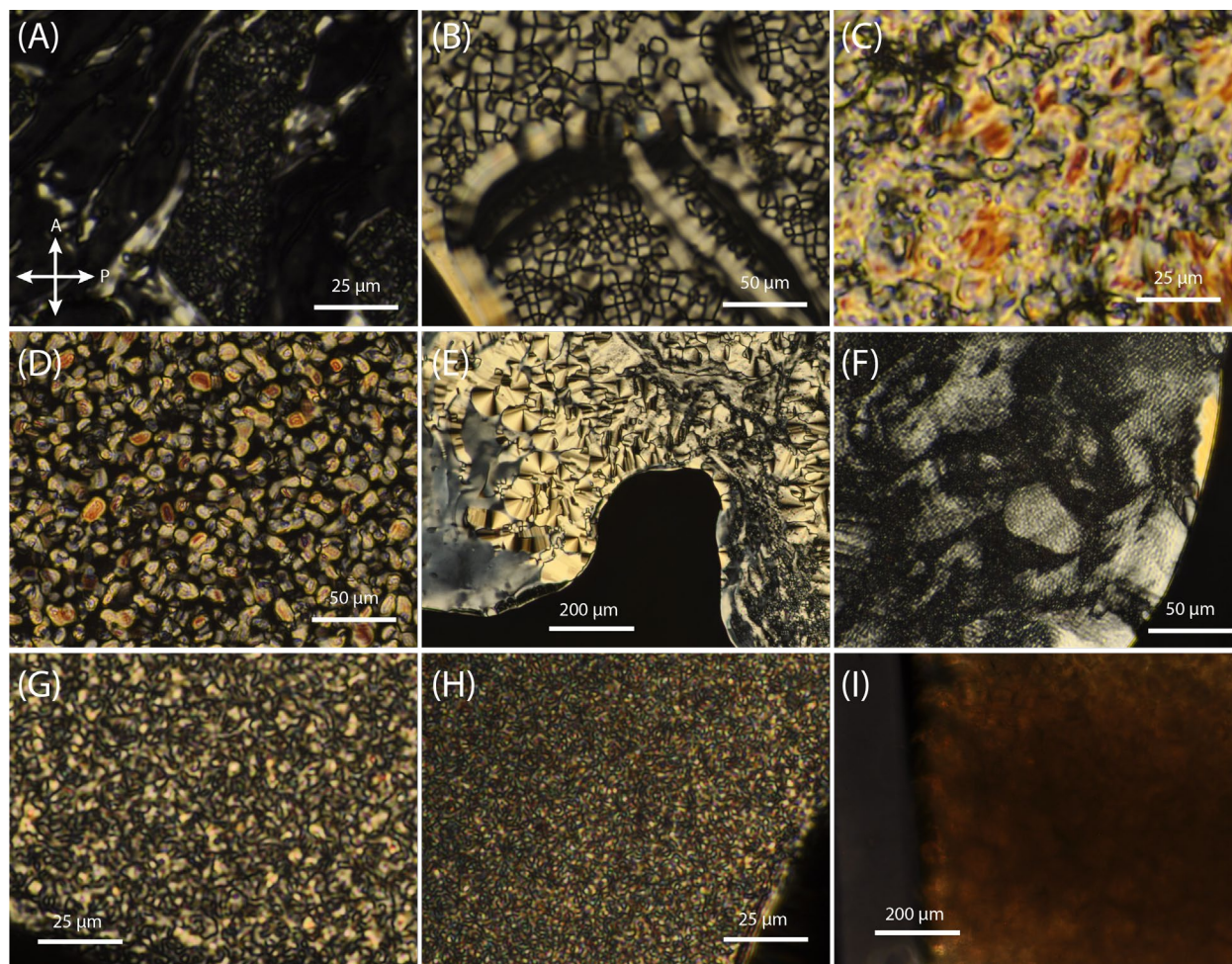


Figure S12: In addition to the usual textures, GCCG shows a variety of optical textures that are not typical of nanoDNA LC. (A) Texture prepared at a concentration near 350 mg/mL. This texture shows characteristic DNA oily streaks, indicating a cholesteric phase, but includes a highly complex topological substructure that appears as fine clusters of point-like objects that may be complicated defect structures. Oily streak patterns can be observed to flow within the cell next to the topological ambiguities that do not appear as fluid. The phase appears like a coexistence between two domain types. (B) Preparation near 400 mg/mL showing cholesteric fingerprint type textures. With small changes in temperature, the fingerprints broke into the complex pattern seen in the image, which resembles strangely a disordered parabolic focal conic texture atop fingerprints that then coarsened back into cholesteric fingerprints, but retaining complicated defect patterns. (C) Preparation near 420 mg/mL showing a complicated coexistence between apparently cholesteric and columnar textures. Typical DNA columnar fan textures were not observed in this sample, but some patches appear to be high order with extinction brushes that are homogenous in direction across the patch. Also present were nodular structures that

appeared to be complicated cholesteric structures similar to those seen in (A). The structures in this sample did not appear to flow when observed over time. (D) Preparation near 450 mg/mL involving a brief excursion to high temperature to melt to isotropic followed by a long incubation at near room temperature that was observed in time-lapse for four days. The resulting texture appears to be a phase separation between a poorly birefringent phase that may well be BCCX and what might be columnar platelets. (E) Preparation near 420 mg/mL showing the range of classic nanoDNA LC textures, including colored cholesteric at left bordering columnar fan textures at the middle of the image. At the lower right corner is a more complicated texture that appears to contain structure that is more what is seen like (C). The sample has a history that suggests a wide concentration gradient with the phase at left having formed after flowing out of the region to the right; it's possible that counterions are sequestered non-uniformly across the cell, giving rise to textures that are more or less dependent on such ions relative to the position where the textures formed. (F) Preparation near 420 mg/mL, allowed to coarsen. The initial texture in this cell appeared to be a dense version of the topologically complex cholesteric seen in (A) and gradually formed what appears to be a coexistent columnar texture as a layer underneath the initial cholesteric. The cholesteric with the complicated nodular structure seemed highly stable and lasted nearly unchanged for several days as the columnar began to appear with it. (G,H) Preparations above 500 mg/mL, in a region of the phase diagram known to contain BCCX; concentrations are not perfectly accurate because the samples were transferred by spatula after being made, allowing them to suffer some evaporation before being sealed in the microscopic cell. Both of these figures contain very complicated textures that are birefringent, but show few characteristics homologous to the columnar nanoDNA phases with which we are familiar. (F) started out as a mostly dark texture with some birefringent spots and then became the texture in the image after a temperature cycle melting it to isotropic at 85° C. (G) is similar, but began in texture shown. (I) A capillary with GCCG at 450 mg/mL after sitting for weeks at room temperature; this capillary is the lowest concentration sample observed in XRD to contain BCCX and we believe the blocks here to be a highly coarsened version of the BCCX phase.

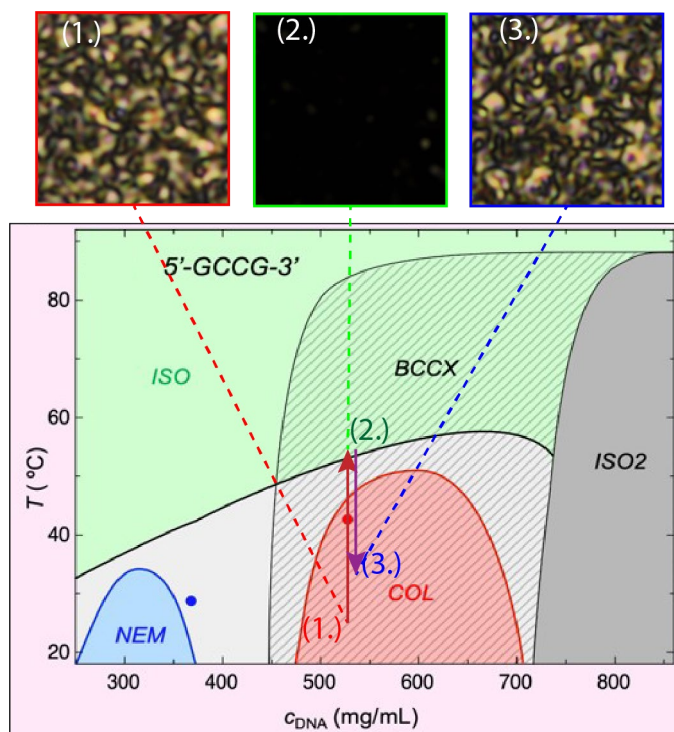


Figure S13 A high concentration sample as seen in *Fig.S12G* was treated to a simple, low magnitude thermocycle. Starting at (1), the sample is ramped in temperature very gently up to (2) and allowed to sit. The birefringence decreases, but a dark phase with little birefringence remains. XRD experiments at similar concentrations have shown the apparent disappearance of coexisting columnar correlations at a lower temperature with BCCX phase persisting to much higher temperatures before also melting. We think that the dark texture seen here is an uncoarsened version of BCCX. The sample here is then ramped in temperature back down below the apparent phase transition line to (3) and the complex texture initially seen reforms. It is important to point out that if this sample is ramped clear to the clearing temperature where the BCCX melts, textures do not reform in the same way when ramped back down to the initial temperature. For open cells as seen here, this phenomenon was difficult to observe because ramping temperature high enough to melt BCCX irretrievably damages the cell by driving water out through evaporation. For flame-sealed capillaries we were able to perform the entire temperature ramp cycle repeatably, showing that the apparent temperature at which birefringent phases melt gradually shifts toward higher and higher temperatures depending on a longer and longer incubation at the lower temperature. This suggests a kinetic process where different competing assembly routes lead to different textures depending on the history of the sample; a faster but less stable assembly route (which we think to be W-C base pairing) produces early textures while a slower but more energetically stable route (which we think to be ion-dependent guanine-guanine oligomerization) then eventually takes over and comes to dominate at later times.

Supplement references

- 1 Fraccia, TP Smith, GP Bethge, L Zanchetta, G Nava, G Klussman, S Clark, NA Bellini, T Liquid crystal ordering and isotropic gelation in solutions of four-base-long DNA oligomers *ACS Nano* **10**, 8508-8516 (2016).
- 2 Podgornik R, Strey HH, Parsegian VA, Colloidal DNA *Curr. Opin. Colloid Interface Sci.* **3**, 534-539 (1998).
- 3 Strey, HH, Parsegian, VA Podgornik, R, Equation of state for polymer liquid crystals: theory and experiment *Phys Rev E* **59**, 999–1008 (1999).
- 4 Nakata, M Zanchetta, G Chapman, BD Jones, CD Cross, JO Pindak, R Bellini, T, Clark, NA End-to-end stacking and liquid crystal condensation of 6 to 20 base pair DNA duplexes *Science* **318**, 1276–1279 (2007).
- 5 Smith GP, Liquid crystals formed by short DNA oligomers and the origin of life, Ph.D. Thesis, University of Colorado, Boulder (2018).
- 6 Podgornik R, Strey HH, Gawrisch K, Rau DC, Rupprecht A, Parsegian VA, Bond orientational order, molecular motion and free energy of high density DNA mesophases. *Proc Natl Acad Sci* **93**, 4261-4266 (1996).
- 7 Podgornik R, Rau DC, Parsegian VA, DNA Parametrization of direct and soft steric-undulatory forces between double helical polyelectrolytes in solutions of several different anions and cations *Biophysical Journal* **66**, 962-971 (1994).
- 8 Zanchetta, G Nakata, M, Buscaglia, M Clark, NA & Bellini, T Liquid crystal ordering of DNA and RNA oligomers with partially overlapping sequences *J Phys Condens Matter* **20**, 494214 (2008).
- 9 Zanchetta, G Nakata, M Buscaglia, M Bellini, T & Clark, NA Phase separation and liquid crystallization of complementary sequences in mixtures of nanoDNA oligomers *Proc Natl Acad Sci* **105**, 1111–1117 (2008).
- 10 Wing R, Drew H, Takano T, Broka C, Tanaka S, Itakura K, Dickerson, RE, Crystal structure analysis of a complete turn of B-DNA. *Nature* **287**, 755–758 (1980). DOI: 10.1038/287755a0
- 11 Kennard O, Hunter WN, Single-Crystal X-Ray Diffraction Studies of Oligonucleotides and Oligonucleotide-Drug Complexes *Angew. Chem. Int. Ed. Engl.* **30**, 1254-1277 (1991)
- 12 Pieraccini S, Gottarelli G, Mariani P, Masiero S, Saturni L, Spada GP, Columnar Lyomesophases Formed in Hydrocarbon Solvents by Chiral Lipophilic Guanosine-Alkali Metal Complexes, *Chirality* **13**, 7-12 (2001).
- 13 Lyubartsev AP, Nordenskiold L, Monte Carlo Simulation Study of Ion Distribution and Osmotic Pressure in Hexagonally Oriented DNA. *J. Phys. Chem.* **99**, 10373-10382 (1995).
- 14 Hexemer, A. *et al.*, A SAXS/WAXS/GISAXS Beamline with Multilayer Monochromator, *J Phys.*

Conf. Ser. 012007 (2010).

15 Ilavsky, J., Nika – Software for 2D data reduction *J. Appl. Cryst.* **45**, 324-328 (2012).

16 Schneider CA, Rasband WS, Eliceiri KW, NIH Image to Image J: 25 years of image analysis *Nat. Methods.* **9**(7) 671-675 (2012).

17 Abraham MJ, Murtola T, Schulz R, Páll S, Smith JC, Hess B, Lindahl E, GROMACS: High performance molecular simulations through multi-level parallelism from laptops to supercomputers *SoftwareX* **1**, 19-25 (2015).

18 Gaussian 16 revision A.03, Firsich MJ *et al.* Gaussian Inc. Wallingford CT, (2016).

19 Austin A, Petersson G, Frisch MJ, Dobek FJ, Scalmani G, Throssell K, “A density functional with spherical atom dispersion terms,” *J. Chem. Theory and Comput.* **8**, 4989 (2012).